Chapter 3
Morphology and Structure of Surfaces, Interfaces and Thin Films

To begin with, it will be useful to give a brief definition of the terms *morphology* and *structure*. The term morphology is associated with a macroscopic property of solids. The word originates from the Greek *μορφή*, which means form or shape, and here it will be used to refer to the macroscopic form or shape of a surface or interface. Structure, on the other hand, is associated more with a microscopic, atomistic picture and will be used to denote the detailed geometrical arrangement of atoms and their relative positions in space.

The distinction between the two terms, however, is sometimes not so clear, even in the case of a clean, well-defined surface prepared in UHV (Chap. 2). What we consider as morphology, i.e. as shape, depends on the type of property being considered and on the resolution of the technique used for its observation. Furthermore, the atomistic structure may often determine, or at least have a significant influence on, the morphology of an interface. For example, details of the interatomic forces determine whether a metal deposited on a semiconductor surface grows layer by layer or whether islands are formed. It is thus necessary to consider both aspects, morphology and structure, in a little more detail. For this purpose one has to approach the problem of an interface from both macroscopic and atomistic viewpoints.

3.1 Surface Stress, Surface Energy, and Macroscopic Shape

The most general macroscopic approach to a problem in the physics of matter is that of thermodynamics. Indeed, there are thermodynamic rules which govern the macroscopic shape and therefore the formation of a particular type of surface or interface of a solid to an adjacent medium or the vacuum. Basic concepts in this context are those of the free specific energy of a surface or interface and that of *surface stress* (sometimes called *surface tension*). These concepts were developed originally by Gibbs [3.1] in his theoretical treatment of a gas/solid (non-crystalline) interface. In this treatment a distinction between *surface free energy* and surface tension was not necessary because a crystalline structure of the solid with tensorial elastic prop-

H. Lüth, *Solid Surfaces, Interfaces and Thin Films*, 5th ed., Graduate Texts in Physics,
DOI 10.1007/978-3-642-13592-7_3,

erties was not considered. For crystalline solids elasticity theory yields the adequate continuum description in terms of the elastic stress tensor $\tau_{ij} = \partial f_i / \partial a_j$ with df_i the differential force in i direction on an area element da_j with normal in j direction and $\varepsilon_{ij} = \partial u_i / \partial x_j$, the strain tensor with du_i the length change of a volume element in i direction upon a position change dx_j in j direction.

When a surface is created, the electrons respond to the absence of atoms above the surface so that the charge distribution near the surface, i.e., details of the chemical bonds, becomes different from that in the bulk. On the atomic scale forces on the atoms in the topmost atomic layers are changed with respect to the bulk situation. The stress tensor τ_{ij} therefore varies along an axis z perpendicular to the surface within several atomic distances. One therefore can define a surface stress tensor (Fig. 3.1) by [3.3, 3.4]

$$\tau_{ij}^{(\mathrm{s})} = \int_{-\infty}^{\infty} dz \left[\tau_{ij}(z) - \tau_{ij}^{(\mathrm{b})} \right]. \tag{3.1}$$

where $\tau_{ij}^{(\mathrm{b})}$ is the bulk stress tensor away from the surface at $z = 0$ and $\tau_{ij}(z)$ describes the spatial variation of stress along z, when one approaches the surface from inside the bulk ($z < 0$). The tensor components which refer to the x- and y-axes are denoted as i and j, respectively. The total surface-induced stress change relative to the bulk, i.e., the integral along z from deep in the bulk into the vacuum $z \to \infty$, is the surface stress (3.1), the dimension of which is force per unit length rather than force per area as in the case of bulk stress. Within the bulk $\tau_{ij}(z)$ equals $\tau_{ij}^{(\mathrm{b})}$ and the surface stress (3.1) vanishes; it has non-vanishing values only within a thin surface film of several atomic layers.

The sign of the surface stress is positive if the surface would like to contract under its own stress, i.e., work is required to stretch the surface elastically (tensile stress). Negative surface stress ($\tau_{ij}^{(\mathrm{s})} \leq 0$) is called compressive. Typical surface stresses of solids are of the order of 1 N/m and are confined to typical distances of 1 nm from the surface.

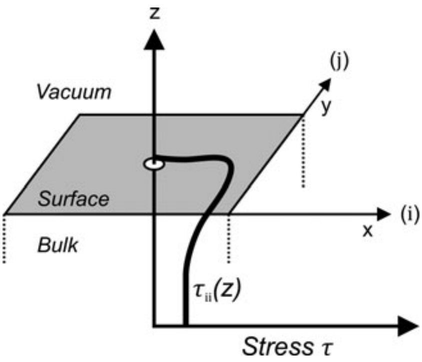

Fig. 3.1 Illustration of the variation of the bulk stress $\tau_{ij}(z)$ near the surface (*solid bold line*) which defines the surface stress according to (3.1). The indices i and j denote the components of the stress tensor in the x and y direction, respectively

In order to define the *specific surface free energy* we consider the work δW which is involved in straining a thin crystal plate of a thickness t by a strain $\delta\varepsilon_{ij}$:

$$\delta W = A \int_{-t/2}^{t/2} dz \sum_{ij} \tau_{ij}(z)\delta\varepsilon_{ij} \tag{3.2}$$

A is the surface area of the slab and z is directed normal to the surfaces. Under the boundary conditions of constant temperature and constant particle number δW equals the change in surface free energy $\delta F^{(\mathrm{s})}$. By means of (3.1) we can split (3.2) into a bulk and a surface contribution:

$$\begin{aligned}\delta W &= \delta W^{(\mathrm{s})} + \delta W^{(\mathrm{b})} = \delta F^{(\mathrm{s})} + \delta F^{(\mathrm{b})} \\ &= 2A \sum_{ij} \tau_{ij}^{(\mathrm{s})}\delta\varepsilon_{ij} + At \sum_{ij} \tau_{ij}^{(\mathrm{b})}\delta\varepsilon_{ij}\end{aligned} \tag{3.3}$$

The factor 2 in the first term is because of the two surfaces, one on each side of the slab. The specific surface free energy γ is introduced by the differential of the surface free energy $F^{(\mathrm{s})}$:

$$\delta F^{(\mathrm{s})} = \delta(\gamma A) = \gamma\delta A + A\delta\gamma \tag{3.4}$$

This means that the surface free energy $F^{(\mathrm{s})}$ may change by two different contributions. When γ stays constant but the surface area changes by δA (first term), the number of surface atoms is changed with a fixed average area per surface atom. The second contribution $A\delta\gamma$ describes the effect that the number of surface atoms remains constant but their energetics, i.e., the interatomic distances in a reconstruction change, varies. When we now specify a particular strain component $\delta\varepsilon_{ij}$ in the first sum of (3.3) and take into account that $dA = A\sum_i d\varepsilon_{ii}$, we obtain, from a comparison of (3.4) with (3.3), the following relation between surface stress $\tau^{(\mathrm{s})}$ and the surface free energy γ:

$$\tau_{ij}^{(\mathrm{s})} = \gamma\delta_{ij} + \frac{\partial\gamma}{\partial\varepsilon_{ij}} \tag{3.5}$$

This relation is called *Shuttleworth equation* [3.5]. For the surface of a liquid the specific surface free energy γ is identical to the (isotropic) surface stress τ, since in a liquid there is no resistance to plastic deformation and the second term in (3.5) vanishes. In a liquid there is neither a resistance to a flow of atoms from the bulk to the surface. For solid surfaces such an atom flow to the surface depends on details of the surface energy and surface stress in that surface spatial region, where the atoms have to be built in. We therefore can consider the term $\partial\gamma/\partial\varepsilon = \tau^{(\mathrm{s})} - \gamma$ as a thermodynamic driving force to move atoms from the bulk into the surface layer. For $\tau^{(\mathrm{s})} - \gamma > 0$ the surface wants to accumulate more atoms than are found in the bulk in a comparable volume. When $\tau^{(\mathrm{s})} - \gamma < 0$ the surface prefers less atoms in the surface layer. In this sense the quantity $\partial\gamma/\partial\varepsilon$ is also one driving force for the formation of certain surface reconstructions, where the surface atomic configuration differs from that in the bulk crystal (Sects. 3.2 and 3.3).

From (3.2 to 3.4) it is clear that the surface energy γ may be regarded as an excess free energy per unit area. It is the reversible work of formation of a unit area of surface or interface at constant system volume, temperature, chemical potential, and number of components. The reversibility requirement in the definition of γ implies that the composition and atomic configuration in the interface region are those of thermodynamic equilibrium.

Some more words to the physical origin of this surface energy γ. If we consider a crystalline structure with its surface next to vacuum, it costs energy to generate an additional piece of surface while keeping the crystal volume and the number of constituent atoms constant. Bonds between neighboring atoms must be broken in order to expose new atoms to the vacuum. The formation of surface defects including steps might also be involved in forming the new surface area. All these effects contribute to the excess surface free energy γ. For crystalline materials, most surface properties depend on the orientation. In particular, depending on the surface orientation (*hkl*) more or less bonds have to be broken to create a piece of surface (Sect. 2.2); also the effect of charge compensation is completely different for polar and nonpolar surfaces of the same crystal (Sect. 2.2). The surface free energy of crystals $\gamma(\boldsymbol{n})$ is therefore strongly dependent on the orientation of the particular surface, $\boldsymbol{n}$. The equilibrium shape of a crystal is not necessarily that of minimum surface area, it may be a complex polyhedron. What then determines the macroscopic shape of solid matter at constant temperature with a fixed volume and chemical potential? From the requirement of minimum free energy one obtains as a necessary condition

$$\int_A \gamma(\boldsymbol{n})\mathrm{d}A = \text{minimum.} \tag{3.6}$$

Thus questions concerning the morphological stability of certain surfaces and the equilibrium shape of materials involve a detailed knowledge of the surface energy $\gamma(\boldsymbol{n})$ and its orientational dependence (γ as a function of lattice plane (*hkl*) or surface normal $\boldsymbol{n}$).

In contrast to fluid interfaces, where the surface energy or tension can usually be obtained quite easily by capillary, and similar experimental techniques, the determination of $\gamma(\boldsymbol{n})$ for the solid–vapor interfaces is difficult. Accordingly, not much reliable experimental information about γ can be found in the literature at present. Some theoretical data according to Bechstedt [3.6] are compiled in Table 3.1.

In the theory for the crystal equilibrium shape and morphological stability, etc. the Wulff plot of $\gamma(\boldsymbol{n}) = \gamma(hkl)$ plays an important role [3.7, 3.8]. As shown in Fig. 3.2, the scalar surface energy γ is plotted in polar coordinates versus the angle Θ between a particular fixed direction and the normals to the (*hkl*) planes. The length of the vector from the origin to a point on the plot represents the magnitude of $\gamma(hkl)$, and the direction is that of the normal to the (*hkl*) plane. Because of (3.6) one can obtain the equilibrium shape of a crystal by connecting those lattice planes

Table 3.1 Calculated surface energies γ (in J/m^2) of low index surfaces of some semiconductors with diamond and zincblende structure as well as of some bcc (Mo, W) and fcc (Al, Au) metals. For the semiconductors the reconstructed and for the metals the relaxed surfaces are considered. In the (311) column the value for the $(\overline{1}\overline{1}\overline{1})$ surface [(211) surface] of InAs [Mo, W] is listed. In the compound case the anion chemical potential is fixed at $\mu_{\mathrm{As}} = \mu_{\mathrm{As}}^{\mathrm{bulk}} - 0.2\,\mathrm{eV}$. In the case of Si experimental values [3.37] are also given in parenthesis. The compilation of the data was performed by Bechstedt [3.6]

Crystal	(100)	(110)	(111)	(311)	Reference
C	5.71	5.93	4.06	5.51	[3.33]
Si	1.41(1.36)	1.70(1.43)	1.36(1.23)	1.40(1.38)	[3.33]
Ge	1.00	1.17	1.01	0.99	[3.33]
InAs	0.75	0.66	0.67	0.78	[3.34]
Mo	3.34	2.92	3.24	3.11	[3.35]
W	4.64	4.01	4.45	4.18	[3.36]
Al	1.35	1.27	1.20		[3.36]
Au	1.63	1.70	1.28		[3.36]

with minimum surface energy. The procedure of constructing the equilibrium shape by means of the $\gamma(hkl)$, plot is displayed qualitatively in Fig. 3.2. A set of planes, each perpendicular to a radius vector is constructed at the point where it meets the Wulff plot. The inner envelope of the planes then determines the set of surfaces that fulfills (3.6). These surfaces are assumed by the material at equilibrium. For liquids and amorphous solids, where $\gamma(\boldsymbol{n})$ is isotropic, both the Wulff plot and the equilibrium shape are spherical.

As a simple example for the rough calculation of $\gamma(\boldsymbol{n})$ let us consider a two-dimensional crystal with a so-called vicinal surface plane [3.8], i.e. a surface plane which consists of a relatively high number of areas with (01) orientation being separated by steps of atomic height (Fig. 3.3a). Such a surface has an orientation angle of θ against the (01) direction. The more steps we have per unit surface area, the higher $\gamma(\boldsymbol{n}) = \gamma\theta$ will be. The step density can be written as $\tan(\theta/a)$. If now the

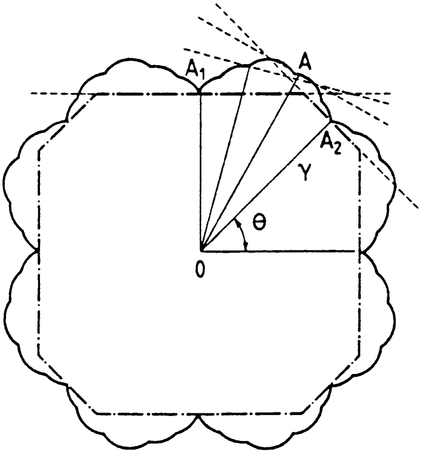

Fig. 3.2 Schematic plot of the scalar surface energy $\gamma(hkl)$ in polar coordinates as a function of angle Θ (describing the normal directions to the $\{hkl\}$ planes). This Wulff construction [3.3, 3.4] yields the equilibrium shape of a solid (dash-dotted) as the inner envelope of the so-called Wulff planes, i.e., the normals to the radius vectors (broken lines)

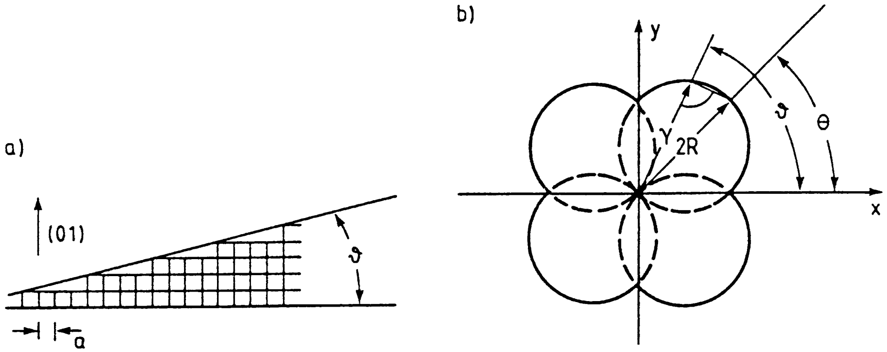

Fig. 3.3 Schematic drawing of surface and simple Wulff plot (surface energy γ in polar coordinates) for a vicinal surface plane with inclination angle θ against [01] consisting of areas with [01] orientation (**a**). The Wulff plot (**b**) consists of circles passing through the origin

surface energy of the low-index plane (01) is set to γ_0 and each step is assumed to make a contribution γ_1 to the total surface energy on the vicinal plane, one might express the surface energy, in general, as a series in the step density $\tan(\theta/a)$

$$\gamma(\theta) = \cos\theta \left[\gamma_0 + \gamma_1 \left(\frac{\tan\theta}{a} \right) + \gamma_2 \left(\frac{\tan\theta}{a} \right)^2 + \dots \right]. \tag{3.7a}$$

The quadratic and higher-order terms describe interactions between steps. Neglecting these interactions for large step distances, i.e. small θ, one gets

$$\gamma(\theta) = \cos\theta \left[\gamma_0 + \gamma_1 \left(\frac{\tan\theta}{a} \right) \right] = \gamma_0 \cos\theta + \frac{\gamma_1}{a} \sin\theta. \tag{3.7b}$$

According to the definition of γ in the Wulff plot as a radius vector from the origin, (3.7b) describes, within that polar plot, a circle (or sphere in three dimensions) passing through the origin. This can, e.g., be shown by considering such a circle (Fig. 3.3b) with diameter $2R$ and inclination Θ with respect to the x-axis. Its mathematical description is

$$\gamma = 2R\cos(\theta - \Theta) = 2R[\cos\Theta\cos\theta + \sin\Theta\sin\theta], \tag{3.8}$$

which is identical to (3.7b), and also enables a geometrical interpretation of γ_0 and γ_1/a. Taking into account the whole range of possible θ values (four quadrants in the plane) a Wulff plot as in Fig. 3.3b results from (3.7b). This is, of course, a rough model in which all higher-order interactions, e.g. interactions between steps, are neglected. More realistic models yield Wulff plots which consist of a number of circles or spheres, as depicted qualitatively in Fig. 3.2.

For real surfaces the surface energy has enormous importance for a number of questions related to surface inhomogeneities. If there are certain lattice planes with particularly low surface energy, a surface can lower its total free energy by exposing areas of this orientation. Thus, even though facetting produces an increase in total surface area, it may decrease the total free energy and is sometimes thermodynamically favored. Also the appearance of surface segregations might be described in terms of minimizing the total free energy of a surface by exposing patches of particularly low surface energy.

As a last remark, an intuitively reasonable, but rough estimation for the surface energy γ of a material is given as follows: the surface energy γ per atom is approximately equal to half the heat of melting per atom. This relation results from the consideration that melting involves the breaking of all the chemical bonds of an atom, whereas γ is related to breaking only about half of the bonds of a surface atom.

3.2 Relaxation, Reconstruction, and Defects

We now move on to consider in a little more detail the atomic structure of a surface. It can easily be seen that on a surface, due to the absence of neighboring atoms on one side, the interatomic forces in the uppermost lattice planes are considerably changed. The equilibrium conditions for surface atoms are modified with respect to the bulk; one therefore expects altered atomic positions and a surface atomic structure that usually does not agree with that of the bulk. Thus a surface is not merely a truncation of the bulk of a crystal. The distortion of the ideal bulklike atom configuration due to the existence of a surface will be different for metals and for semiconductors. In metals we have a strongly delocalized electron gas and a chemical bond which is essentially not directed, whereas in tetrahedrally bonded semiconductors (Si, Ge, GaAs, InP, etc.) significant directional bonding is present. Bond breaking on one side due to the surface is expected to have a more dramatic effect on the atomic configuration at the surface of a semiconductor.

Figure 3.4 illustrates schematically some characteristic rearrangements of surface atoms. A pure compression (or possibly extension) of the topmost (or top few) interlayer separations) normal to the surface is called *relaxation*. In this case, the 2D lattice, i.e. the periodicity parallel to the surface within the topmost atomic layer is the same as for the bulk. More dramatic changes of the atomic configuration, as shown in Fig. 3.4b, usually related to shifts parallel to the surface, can change the periodicity parallel to the surface. The 2D unit mesh has dimensions different from those of a projected bulk unit cell. This type of atomic rearrangement is called *reconstruction*. In reconstructions the surface unit mesh must not necessarily be changed with respect to the bulk, only the atomic displacements from their bulk positions must be more complex than a pure shift normal to the surface as in Fig. 3.4a. As an example we will consider below the cleaved GaAs(110) surface. Reconstructions also include surface atomic configurations in which atoms or a whole row of atoms are missing in comparison with the bulk (Fig. 3.4c). In this case the surface periodicity is always different from that of the bulk.

As was already mentioned above, semiconductor surfaces with their strongly directional covalent bonding character often show quite complex reconstructions. Up to now it has been a difficult task to determine the atomic positions of these reconstructed surfaces experimentally. Usually, a variety of methods [LEED (Panel VIII: Chap. 4), ARUPS (Sect. 6.3), Rutherford backscattering (Sect. 4.11),

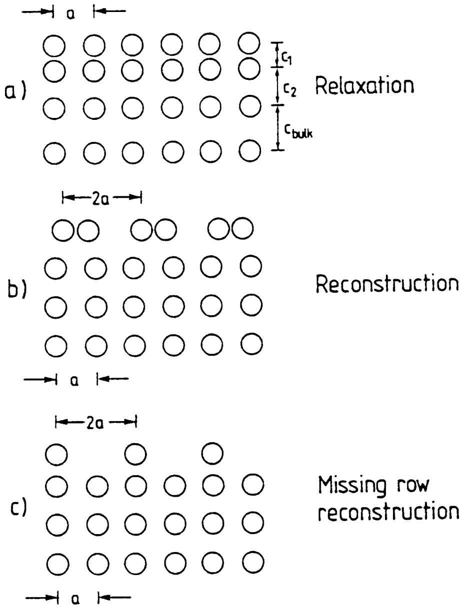

Fig. 3.4 a–c Schematic side view of the characteristic rearrangements of surface atoms of a simple cubic lattice with lattice constant a: (**a**) Relaxation of the topmost atomic layer normal to surface (different lattice spacings c); (**b**) reconstruction of the topmost atomic layer into a surface net with double periodicity distance $2a$; (**c**) missing row reconstruction with missing atoms in the topmost lattice plane

etc.] have to be applied to arrive at an unequivocal structural model. One of the well-understood examples is the clean cleaved GaAs(110) surface which exhibits in LEED the same surface unit mesh as one would expect for a truncated bulk crystal. Nevertheless, the atomic positions at the surface are quite distorted with respect to the bulk (Fig. 3.5). Compared with their bulk positions the As atoms of the topmost atomic layer are raised, whereas the neighboring Ga surface atoms are pushed inwards. There is a tilt in the surface Ga–As bond of about 27° to the surface and only small changes in the Ga–As bond lengths [3.9]. In this particular case of GaAs(110) the reconstruction develops just by simple shifts of surface atoms involving tilting of covalent bonds. An even stronger perturbation of the lattice including bond breaking and reformation of new bonds is found on the Si(111) surface when prepared by cleavage in UHV. In the $[0\bar{1}1]$ direction the (2 × 1) LEED pattern indicates a double periodicity distance in real space. The reconstruction model which has become established for this type of surface is shown in Fig. 3.6 (more details are given in Sect. 6.5). The Si atoms on the surface are rearranged in such a way that neighboring dangling bonds can form zig-zag chains of π-bonds, similar to a long-chain organic molecule [3.10]. Atoms of the next deeper atomic layers also have to change their positions and participate in the reconstruction. Detailed self-consistent total energy calculations reveal that in spite of bond breaking, this so-called π-bonded chain model fulfills the requirement of minimum total energy with respect to other, may be more obvious, atomic configurations. According to the present state of knowledge, a slight buckling, i.e. outward and inward shift of neighboring Si surface atoms also has to be assumed (Fig. 3.2).

One might enquire a little deeper into the reasons for relaxation and reconstruction. As the examples on semiconductor surfaces show, there is certainly a tendency

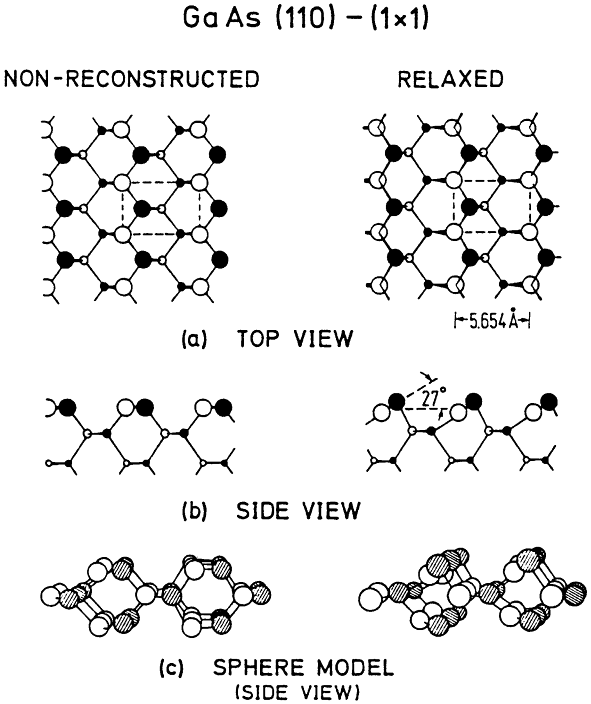

Fig. 3.5 a–c Atomic positions of the GaAs(110) surface; ideal, non-reconstructed and relaxed as it appears after cleavage in UHV. (**a**) Top view; the (1 × 1) unit mesh is plotted as a broken line. (**b**) Side view. (**c**) Sphere model. (Open circles designate Ga atoms and shaded circles As. Smaller circles indicate deeper atomic layers

to saturate free dangling bonds by forming new bonds within the surface [Si(111)-(2 × 1)]. This can lead to an overall decrease of the surface free energy. On the surface of a polar semiconductor like GaAs the undisturbed dangling bonds of Ga and As surface atoms carry charge and an overall decrease of surface energy is achieved by an electronic charge transfer from the Ga to the As dangling bond. The Ga dangling bond becomes more sp^2-like whereas the As bond gets more p_z character thus causing the inwards and outwards shifts of the corresponding atoms.

On metal surfaces there are usually no directional bonds, and other mechanisms might be imagined which give rise to surface relaxation and reconstruction. Figure 3.7 exhibits in a schematic way the rigid ion core positions near a metal surface. The free electrons are delocalized between the ion cores making an electrically neutral object. In order to ensure such a neutrality one can formally attribute to each core a Wigner-Seitz cell (squares in Fig. 3.7a), which contains the corresponding electronic charge.

On a surface, as depicted in Fig. 3.7a, this would lead to a rapidly varying electron density at the surface, thus increasing the kinetic energy of the electrons in proportion to the square of the derivative of the wave function. As indicated in Fig. 3.7a, the surface electronic charge therefore tends to smooth out and to form a surface contour (broken line) which gives rise to the formation of a surface electronic dipole contributing to the work function of that particular surface (Sect. 10.3). On the other hand, due to this dipole layer, the positive ion cores in the topmost

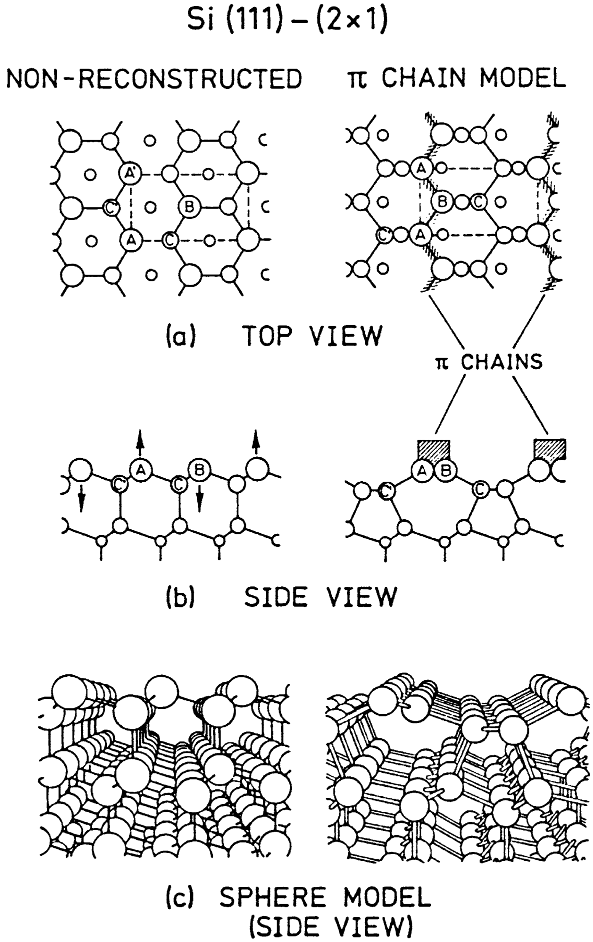

Fig. 3.6 a–c Atomic positions at the Si(111) surface; ideal, non-reconstructed and with (2 × 1) reconstruction (π-bonded chain model) as occurs after cleavage in UHV. The shaded areas denote the location of the chains originating from overlap between neighboring dangling bonds. (**a**) Top view, the (2 × 1) unit mesh is plotted in broken line. (**b**) Side view; arrows indicate possible up- and downwards shifts of surface atoms of type A and B, which give rise to the so-called buckling reconstruction. (**c**) Sphere model. (Smaller circles indicate deeper atomic layers)

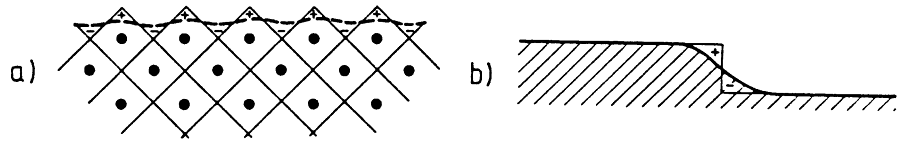

Fig. 3.7 Schematic representation of the formation of electronic surface dipoles at metal surfaces (**a**) by smearing out of the electronic charge distribution of the Wigner Seitz cells at the surface (rectangles), and (**b**) by smearing out of the electronic charge distribution at a step

Table 3.2 Compilation of some clean metal surface relaxations. As can be seen, the topmost lattice plane distance is generally contracted by several percent of the unrelaxed value [3.8]

Surface	Spacing change of top layer [%]
Ag(110)	−8
Al(110)	−10
Cu(100)	0
Cu(110)	−10
Cu(311)	−5
Mo(100)	−12.5

atomic layer feel a net repulsion from the charge in their Wigner Seitz cell, and an inwards displacement results. This effect is thought to be one possible source of the contraction (relaxation) of the topmost lattice plane observed on many metal surfaces (Table 3.2). Apart from this relaxation, most low-index metal surfaces do not exhibit a reconstruction, i.e. their surface unit mesh equals that of the bulk.

As is the case in the bulk, ideal surfaces with complete translational symmetry cannot exist for entropy reasons. On a real surface *defects* are always found. One can classify surface defects according to their dimensionality (Fig. 3.8). The terraces represent portions of low-index planes. Zerodimensional or point defects involve adatoms, ledge adatoms, kinks and vacancies. For a clean monatomic crystal (Si, Ge, Al, etc.) this characterization seems sufficient. Looking via an atomic scale, in particular on a surface of a compound crystal (GaAs, ZnO, etc.), one can distinguish, in more detail, between adatoms of the same kind (e.g., Ga or As on GaAs) or foreign adatoms (Si on GaAs, etc.); adatoms might be bonded on top of the uppermost atomic layer or they might be incorporated into the topmost lattice plane as interstitials. Vacancies, too, might have varying character on an atomic scale. On a GaAs surface, for example, both Ga and As vacancies may exist. Due to the different ionic charge of the missing atoms, the two types of vacancies exhibit different electronic properties (Sects. 6.2, 6.3). Another type of zerodimensional defect characteristic of compound semiconductor surfaces is the so-called *anti-site defect*, where in GaAs, for example, an As atom occupies a Ga site ($\mathrm{As}_{\mathrm{Ga}}$) or vice versa ($\mathrm{Ga}_{\mathrm{As}}$). As is easily seen from the different electron orbitals and the type of chemical bonding, anti-site defects also give rise to electrically active centers (Sects. 6.2, 6.3).

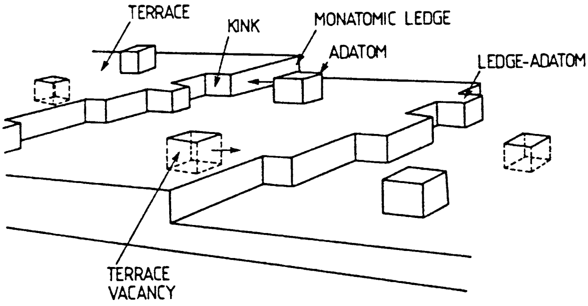

Fig. 3.8 Schematic drawing of various defects that may occur on a solid surface

An important one-dimensional or line defect is the step in which the ledge (Fig. 3.8) separates two terraces from each other. In many cases steps of single atomic height prevail. Depending on the orientation of the step and of the corresponding terraces, step atoms expose a different number of dangling bonds as compared with atoms in the terraces. Steps are important in the formation of vicinal surfaces (high-index surfaces), i.e. surfaces which are oriented at a small angle with respect to a low-index surface. Such vicinal surfaces are formed by small low-index terraces and a high density of regular steps (Fig. 3.3a). Steps often have interesting electronic properties. On semiconductors with strongly covalent bonds, the different dangling bond structure might modify the electronic energy levels near steps. On metal surfaces the free electron gas tends to be smoothed out at the step thus forming dipole moments due to the spatially fixed positive ion cores (Fig. 3.7b).

Other important surface defects are related to dislocations. An edge dislocation penetrating into a surface with the Burgers vector oriented parallel to the surface gives rise to a point defect. Step dislocations hitting a surface also cause point defects which are usually sources of a step line.

Because of the local variation that defects cause in all important surface quantities, such as binding energy, coordination, electronic states, etc., the defect structure of a surface plays a predominant role in processes such as crystal growth, evaporation, surface diffusion, adsorption and surface chemical reactions.

3.3 Two-Dimensional Lattices, Superstructure, and Reciprocal Space

3.3.1 Surface Lattices and Superstructures

Even though real crystalline surfaces always contain point and/or line defects, the model of a perfectly periodic two-dimensional surface is convenient and adequate for the description of well-prepared samples with large well-ordered areas and low defect density. The surface region of a crystal is, in principle, a three-dimensional entity; reconstructions usually extend into the crystal by more than one atomic layer. Space-charge layers on semiconductor surfaces can have a depth of hundreds of Ångstroms (Chap. 7). Moreover, the experimental probes in surface experiments, even slow electrons, usually have a non-negligible penetration depth. But compared to subsurface layers, the topmost atomic layer is always predominant in any surface experiment. As a result, each layer of atoms in the surface is intrinsically inequivalent to other layers, i.e. the only symmetry properties which the surface posesses are those which operate in a plane parallel to the surface. Although the surface region is three-dimensional, all symmetry properties are two-dimensional (2D). Thus surface crystallography is twodimensional and one has to consider 2D point groups and 2D Bravais nets or lattices [3.11].

The point group operations which are compatible with 2D periodicity are the usual 1, 2, 3, 4 and 6-fold rotation axes perpendicular to the surface, and mirror planes, also normal to the surface. Inversion centers, mirror planes and rotation axes parallel to the surface are not allowed, since they refer to points outside the surface. By combining the limited number of allowed symmetry operations, one obtains 10 different *point group symmetries* denoted [3.12]

$$1, 2, 1m, 2mm, 3, 3m, 4, 4mm, 6, 6mm.$$

The numeral $\nu = 1 \ldots .6$ denotes rotations by $2\pi/\nu$ and the symbol m referrs to reflections in a mirror plane. The third m indicates that a combination of the preceding two operations produces a new mirror plane.

The operation of the 2D point groups on a 2D translational net or lattice produces the possible 2D *Bravais lattices*. In contrast to three dimensions, only 5 symmetrically distinct nets are possible (Fig. 3.9). There is only one non-primitive unit mesh, the centered rectangular one. In all other cases a centered unit cell can also be described by a primitive Bravais lattice. Nevertheless, in practice one often uses, e.g., centered square meshes for the convenience of description.

As was mentioned already, surface experiments such as diffraction of low-energy electrons (Panel VIII: Chap. 4) usually probe not only the topmost atomic layer; the information obtained (e.g., in a diffraction pattern) is related to several atomic layers. A formal description of the periodic structure of the topmost atomic layers of a crystalline solid must therefore contain information about the ideal substrate as well as about the one or two topmost atomic layers which might exhibit a different periodicity due to a possible reconstruction or a well-ordered, periodic adsorbate layer (Fig. 3.10). In such a situation, where a different periodicity is present in the topmost atomic layer, a surface lattice, called a *superlattice*, is superimposed on the substrate lattice which exhibits the basic periodicity. The basic substrate lattice can be described by a set of 2D translational vectors

$$\boldsymbol{r}_m = m\boldsymbol{a}_1 + n\boldsymbol{a}_2 \tag{3.9}$$

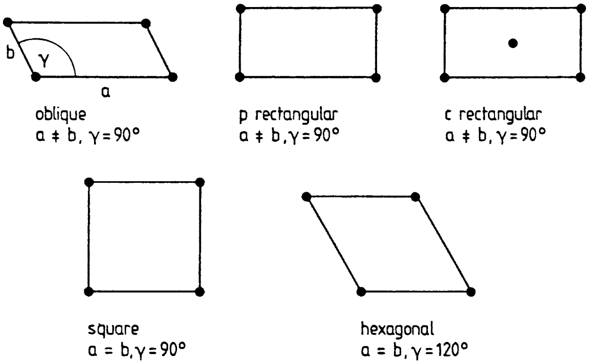

Fig. 3.9 Five possible two-dimensional (2D) Bravais lattices

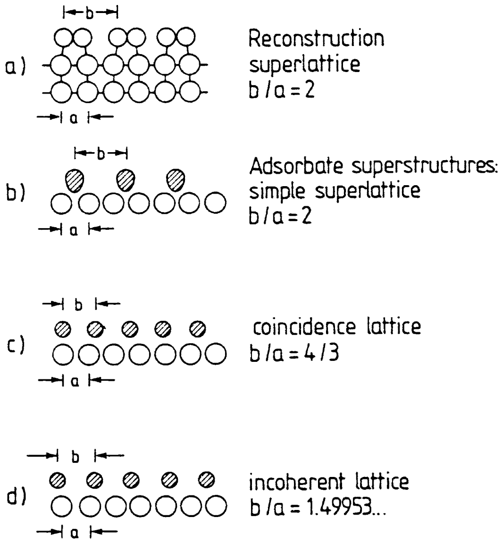

Fig. 3.10 a–d Different possibilities for surface unit meshes which are different from that of the underlying bulk material: (**a**) Reconstruction of a clean surface due to lateral shift of the atoms within the topmost lattice plane. (**b** to **d**) Adsorbate reconstructions with different adsorbate atom–substrate atom lattice constant ratios b/a

where $\boldsymbol{m} = (m, n)$ denotes a pair of integer numbers, and the $\boldsymbol{a}_\mathrm{i}$'s are the two unit mesh vectors. The surface net of the topmost atomic layer may then be determined in terms of the substrate net by

$$\begin{aligned} \boldsymbol{b}_1 &= m_{11}\boldsymbol{a}_1 + m_{12}\boldsymbol{a}_2 \\ \boldsymbol{b}_2 &= m_{21}\boldsymbol{a}_1 + m_{22}\boldsymbol{a}_2 \end{aligned} \quad \text{or} \quad \begin{pmatrix} \boldsymbol{b}_1 \\ \boldsymbol{b}_2 \end{pmatrix} = \boldsymbol{M} \begin{pmatrix} \boldsymbol{a}_1 \\ \boldsymbol{a}_2 \end{pmatrix}, \tag{3.10}$$

where $\boldsymbol{M}$ is a 2×2 matrix, namely

$$\boldsymbol{M} = \begin{pmatrix} m_{11} & m_{12} \\ m_{12} & m_{11} \end{pmatrix}. \tag{3.11}$$

For the areas B and A of the surface and of the substrate unit mesh, respectively, it follows that

$$B = |\boldsymbol{b}_1 \times \boldsymbol{b}_2| = A \det \boldsymbol{M}. \tag{3.12a}$$

The determinant of $\boldsymbol{M}$,

$$\det \boldsymbol{M} = \frac{|\boldsymbol{b}_1 \times \boldsymbol{b}_2|}{|\boldsymbol{a}_1 \times \boldsymbol{a}_2|}. \tag{3.12b}$$

can be used to characterize the relation between surface and substrate lattice (Fig. 3.10). When det $\boldsymbol{M}$ is an integer (Fig. 3.10b), the surface lattice is said to be simply related; it is called a *simple superlattice*. When det $\boldsymbol{M}$ is a rational number (Fig. 3.10c), the superstructure is referred to as a *coincidence lattice*.

In cases where the adsorbate–substrate interaction is much less important than interactions between the adsorbed particles itself, the substrate has no determining influence on the superstructure and the adsorbate lattice might be out of registry with the substrate net. In this case, where det $\boldsymbol{M}$ is an irrational number (Fig. 3.10d), the superstructure is called an *incoherent lattice* or an incommensurate structure.

According to Wood [3.12] there is a simple notation for superstructures in terms of the ratio of the lengths of the primitive translation vectors of the superstructure and those of the substrate unit mesh. In addition, one indicates the angle (if any) through which one mesh is rotated relative to the other. If on a certain substrate surface $X\{hkl\}$ a reconstruction is given with $(\boldsymbol{b}_1 \| \boldsymbol{a}_1 . \boldsymbol{b}_2 \| \boldsymbol{a}_2)$

$$\boldsymbol{b}_1 = p\boldsymbol{a}_1, \quad \boldsymbol{b}_2 = q\boldsymbol{a}_2. \tag{3.13}$$

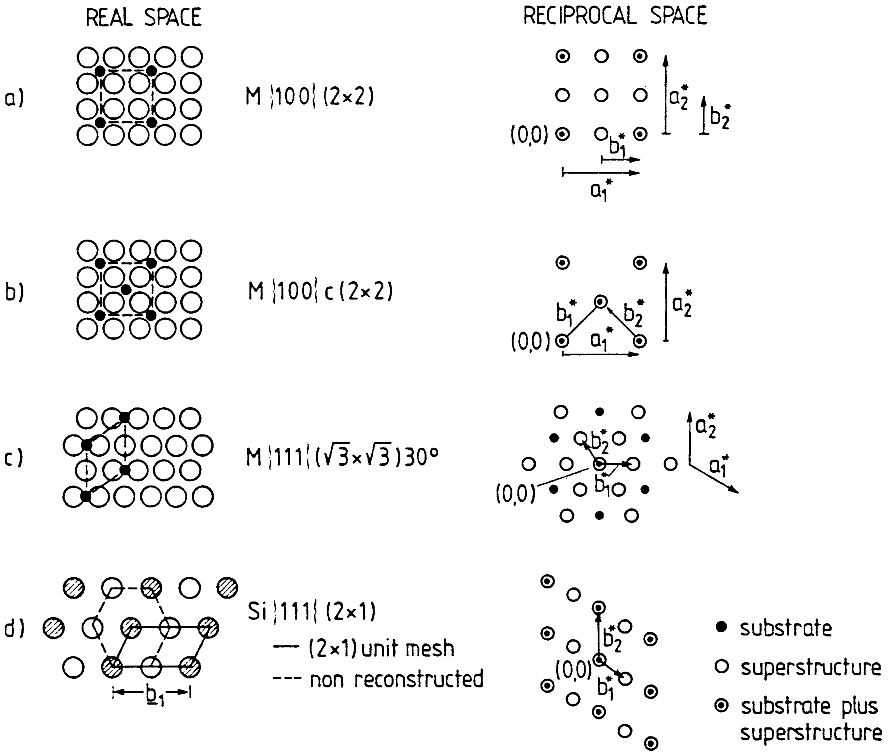

Fig. 3.11 a–d Examples of different superlattices in real space and in reciprocal space: (**a** to **c**) Adsorbed atoms on several low index surfaces of a closed packed metal (M), (**d**) (2 × 1) unit mesh (solid line) of a Si(111) surface prepared by cleavage in UHV

then the notation is given as

$$X\{hkl\}(p \times q) \ \text{or}\ X\{hkl\}\mathrm{c}(p \times q) \tag{3.14a}$$

A possible centering can be expressed by the symbol c. If in the more general case the translational vectors of substrate and of superstructure are not parallel to each other, but rather a rotation by a certain angle $R°$ has to be taken into account, one describes this situation by

$$X\{hkl\}(p \times q) - R°. \tag{3.14b}$$

Some examples of this notation for some adsorbate superlattices on metal surfaces M{100}, M{111} and for the clean Si{111} surface with (2 × 1) superstructure (after cleavage in UHV) are illustrated in Fig. 3.11.

Surface scattering and diffraction experiments are best described in terms of the reciprocal lattice which will be explained in detail in Sect. 3.3.2 and Chap. 4.

3.3.2 2D Reciprocal Lattice

As in three-dimensional space, the translational vectors of the 2D reciprocal lattice, $\boldsymbol{a}_i^*$, are defined in terms of the real-space lattice vectors $\boldsymbol{a}_{\mathrm{i}}$ by

$$\boldsymbol{a}_1^* = 2\pi \frac{\boldsymbol{a}_2 \times \hat{\boldsymbol{n}}}{|\boldsymbol{a}_1 \times \boldsymbol{a}_2|}, \quad \boldsymbol{a}_2^* = 2\pi \frac{\hat{\boldsymbol{n}} \times \boldsymbol{a}_1}{|\boldsymbol{a}_1 \times \boldsymbol{a}_2|}, \tag{3.15}$$

where $\hat{\boldsymbol{n}}$ is the unit vector normal to the surface, i.e.

$$\boldsymbol{a}_i^* \cdot \boldsymbol{a}_j = 2\pi\delta_{ij} \ \text{and}\ |\boldsymbol{a}_i^*| = 2\pi[a_i \sin \sphericalangle(a_i a_j)]^{-1}, \ \ i, j = 1, 2. \tag{3.16}$$

Equations (3.15, 3.16) can be used to construct the reciprocal lattice geometrically to a given 2D network, as displayed in Figs. 3.11.

A general translation vector in reciprocal space is given by

$$\boldsymbol{G}_{hk} = h\boldsymbol{a}_1^* + k\boldsymbol{a}_2^*, \tag{3.17}$$

where the integer numbers h and k are the Miller indices.

In analogy to the real-space relations (3.10–3.12), the reciprocal network of a superstructure $(\boldsymbol{b}_1^*, \boldsymbol{b}_2^*)$ can be expressed in terms of the substrate reciprocal lattice $(\boldsymbol{a}_1^*, \boldsymbol{a}_2^*)$ by

$$\begin{matrix} \boldsymbol{b}_1^* = m_{11}^*\boldsymbol{a}_1^* + m_{12}^*\boldsymbol{a}_2^* \\ \boldsymbol{b}_2^* = m_{21}^*\boldsymbol{a}_1^* + m_{22}^*\boldsymbol{a}_2^* \end{matrix} \quad \text{or} \quad \begin{pmatrix} \boldsymbol{b}_1^* \\ \boldsymbol{b}_2^* \end{pmatrix} = \boldsymbol{M}^* \begin{pmatrix} \boldsymbol{a}_1^* \\ \boldsymbol{a}_2^* \end{pmatrix}. \tag{3.18}$$

The matrices in (3.10, 3.18) are related to one another by

$$\boldsymbol{M}^* = (\boldsymbol{M}^{-1})^T, \tag{3.19a}$$

where $(\boldsymbol{M}^{-1})^T$ is the transpose inverse matrix with

$$m_{ii} = \frac{m^*_{ii}}{\det \boldsymbol{M}^*} \quad \text{and} \quad m_{ij} = \frac{-m^*_{ji}}{\det \boldsymbol{M}^*}. \tag{3.19b}$$

3.4 Structural Models of Solid–Solid Interfaces

The vacuum–solid interface, i.e. the surface considered so far is the simplest interface in which a crystal can participate. Many concepts of surface physics, e.g. that of defects, relaxation (Sect. 3.2), surface states (Chap. 6), surface collective modes such as phonons and plasmons (Chap. 5) etc., can be transferred to more complex interfaces, in particular to the liquid–solid and the solid–solid interface. Important examples of solid–solid interfaces with considerable technological importance are the interfaces in semiconductor heterostructures ($\mathrm{GaAs/Ga}_x\mathrm{Al}_{1-x}\mathrm{As}$, GaAs/Ge, Chap. 8), the $\mathrm{Si/SiO_2}$ interface in a MOS structure (Sect. 7.7), the metal–semiconductor junction (Chap. 8), the interfaces between optical elements and antireflecting coatings or the interface between an organic and an inorganic semiconductor (sensor applications).

In terms of the atomic structure, two main features (on different levels) have to be considered (Fig. 3.12). The interface might be crystalline–crystalline (Fig. 3.12a) or the crystalline substrate might be covered with a non-crystalline amorphous solid

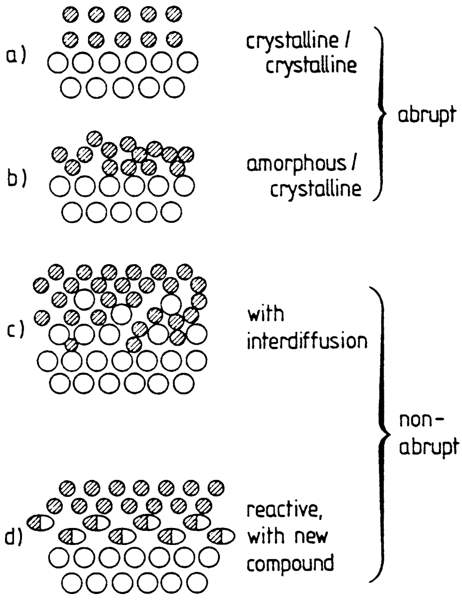

Fig. 3.12 a–d Different types of solid–solid interfaces (film on substrate); substrate atoms depicted as open circles, film atoms as dark circles, reaction compounds (in **d**) as half-dark and half-open symbols

(Fig. 3.12b). Polycrystalline overlayers might form, at least locally, more or less disturbed crystalline–crystalline interfaces (grain boundaries, etc.).

The second important feature is the abruptness of an interface: Solid–solid interfaces, both crystalline–crystalline and crystalline–non-crystalline, might be sharp and abrupt on an atomic scale or they might be "washed out" by interdiffusion (Fig. 3.12c) and/or formation of new chemical compounds (Fig. 3.12d). In such a situation more than two different phases might be in thermal equilibrium with each other. If we consider an interface between two different materials A and B at a certain temperature T_0 the "sharpness" of the interface can be described in terms of the concentrations [A] or [B]. After the materials A and B have been brought into contact at a temperature T_0, [A] might change gradually with distance after some reaction time (Fig. 3.13a, left hand) or an abrupt change in concentration indicates a more or less sharp interface at z_0 (Fig. 3.13b, left hand); here [A] changes abruptly on going from phase I to phase II. The detailed shape of the concentration profiles within the two phases I and II depends, of course, on diffusion constants, reaction rates and on the reaction time during which the materials A and B are in contact at the reaction temperature T_0. Details of the solid–solid chemical reaction which forms the A/B interface are dependent both on kinetic and on thermodynamic aspects. Thermodynamic considerations can yield the limiting conditions for the formation of the particular interface, but not all thermodynamically possible phases will necessarily occur in reality because of kinetic limitations such as high activation energies for nucleation (Sect. 3.5). For analyzing the various possibilities for interface formation, however, thermodynamic parameters are important. Phase

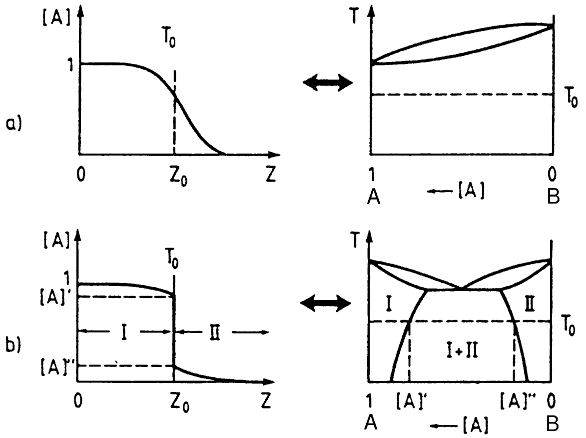

Fig. 3.13 a,b Phase diagrams (right) and concentration versus depth (z) plots (left) for two materials A and B. [A] and [B] denote the concentrations of A and B, respectively. The two materials have been brought into contact at a temperature T_0 and after a certain reaction time the interface at z_0 (left) might be gradual (**a**) or more or less sharp (**b**) depending on the phase diagram (right). In (**a**) the phase diagram allows complete mixing of A and B whereas in (**b**) the phase diagram (right) allows the existence of two separate phases I and II and mixing of I and II at the particular temperature T_0 only between the concentrations [A]′ and [A]″

diagrams can therefore give useful information about the expected properties of certain solid–solid interfaces. For example, a prerequisite for the formation of a smooth gradual interface (Fig. 3.13a) at temperature T_0 is a binary phase diagram, which allows complete mixing of the two components A and B at T_0 (Fig. 3.13a, right). In contrast, a phase diagram as in Fig. 3.13b (right hand) allows mixing of the two components at temperature T_0 only between the concentrations $[A]'$ and $[A]''$: outside this concentration range only the phases I and II exist. Correspondingly a solid-state reaction at T_0 between A and B leads to a sharp interface (Fig. 3.13b. left hand) with an abrupt change from $[A]'$ to $[A]''$ at the very interface at z_0. Of course, such interfaces can also be related to different types of phase diagrams having a miscibility gap. More complex phase diagrams with more than two stable phases (I, II, III, etc.) at a certain temperature might be related to spatially extended solid–solid interfaces with several layered phases I, II, III, etc.

As has already been emphasized, the real atomic structure of a solid–solid interface depends in detail on the atomic properties of the two partners forming the interface. Thermodynamic considerations can only give a rough guide to the general possibilities. In this sense interfaces between two solids are more complex than vacuum solid interfaces, and heterophase boundaries are likewise more complex than homophase interfaces. But even in the latter case of a homophase boundary, where two identical crystalline structures, but with different lattice orientation, touch each other (as in grain boundaries), different atomic models for the interface exist [3.13]. According to L. Brillouin (1898) an *amorphous interlayer*, where the crystalline structure is fully disturbed (liquid-like phase) might be assumed. The idea seems consistent with the intuitive notion that atoms at an interface, as in Fig. 3.14, are in energetically less favorable positions and that a displacement from their crystallographic sites might lead to an energy reduction. This displacement disrupts the crystallographic structure close to the interface and might result in an amorphous interlayer.

Other interface models are based on the concept of *dislocations*, which allow matching of the two half crystals. In Fig. 3.15a a grain boundary is schematically

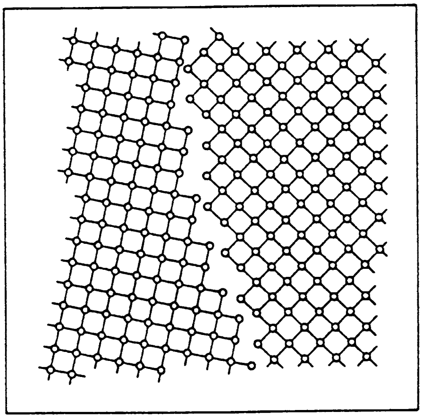

Fig. 3.14 Simplest picture of a solid–solid interface between two differently oriented crystalline domains (domain boundary). The crystallographic structure on each side of the boundary is full retained

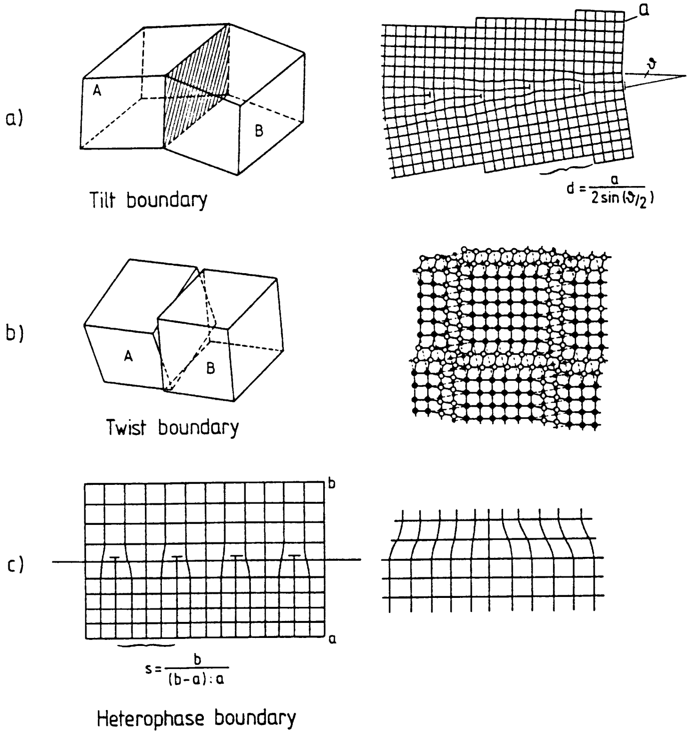

Fig. 3.15 a–c Crystalline interface models (grain boundaries) based on dislocations: (**a**) Tilt boundary due to edge dislocations. (**b**) Twist boundary due to screw dislocations. (**c**) Heterointerface between two different crystalline solids. The lattice mismatch is adjusted by edge dislocations (left) or by strain (right)

depicted in which two tilted, but otherwise identical, crystal halves are separated by a tilt boundary. With θ as the inclination angle and a as lattice constant, the distance s between two edge dislocation is

$$s = a[2\sin(\theta/2)]^{-1} \simeq a/\theta. \tag{3.20}$$

Each dislocation contains a certain amount of elastic energy in its surrounding strain field. The energy stored in such a tilt boundary can thus be calculated by summing up the contributions of the edge dislocations. Similar considerations are valid for the twist boundary (Fig. 3.15b), where screw dislocations are necessary to adjust the two twisted lattices to each other. Another interesting case is the heterophase boundary, which is always found in heteroepitaxy, where a monocrystalline overlayer is grown on a different monocrystalline substrate (see heteroepitaxy of III-V semiconductors in Sect. 2.4). Usually there is a certain lattice mismatch, i.e. a difference between the lattice constants of the two materials. Only below a certain critical value for the mismatch can epitaxy occur. But even in that case the different lattice constants might adjust at the interface by the formation of edge dislocations (Fig. 3.15c). With a and b as the two lattice constants, the distance between dislocations follows as

$$s = \frac{ab}{|b-a|}. \tag{3.21}$$

The energy stored in such an interface between an epitaxial film and its substrate is calculated by summing up the energy contributions of the strain fields of the edge dislocations.

For thinner epitaxial films with low lattice mismatch one might image a different way of matching the various lattice constants, namely by elastic strain, i.e. a deformation of the lattice of the epitaxial film. The type of interface that is actually formed depends on the thickness of the film and on the amount of lattice mismatch. In order to predict the type of lattice matching, by strain only or by formation of edge dislocations, a calculation and comparison of the free energies involved is necessary. In particular, the interaction between dislocations has to be taken into account. If two dislocations approach each other, their strain fields overlap which might lead to a decrease in energy relative to the situation of non-overlapping strain fields (since a given dislocation already provides part of the strain required by its neighbors). Thus for higher lattice mismatch, $(b-a)/a$, the formation of dislocations becomes energetically more favorable than building up lattice strain in the whole layer without formation of dislocations. Qualitatively, and also by use of model calculations [3.14], one thus arrives at relationships between the corresponding energy densities $\overline{E}_\varepsilon$ (with only strain), $\overline{E}_\mathrm{D}$ (with dislocations), and the mismatch and layer thickness h, as shown in Fig. 3.16. Below a critical mismatch ε_0 and below a critical layer thickness h_0 a purely strained epitaxial layer has a lower interface energy than do dislocations. If only dislocations are present, $\overline{E}_\mathrm{D}$ does not change with increasing layer thickness h (Fig. 3.16b), since thicker films are not more stressed than thin ones. On the other hand, with no dislocations present, the total stress energy $\overline{E}_\varepsilon$

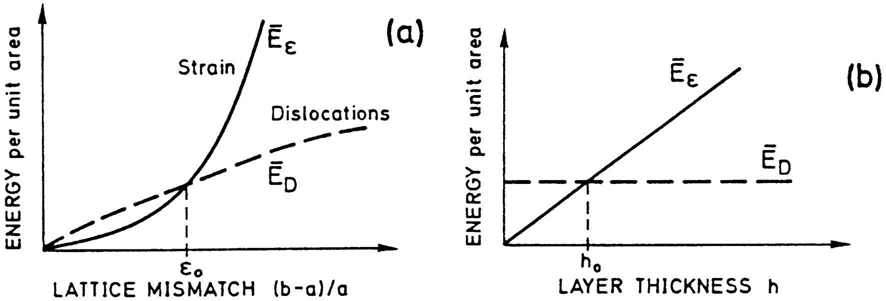

Fig. 3.16 a,b Qualitative plots of lattice energy stored at a crystalline hetero-interface per unit area: (**a**) as a function of lattice mismatch; beyond a critical lattice mismatch ε_0 (a and b are the lattice constants of the two materials) the adjustment of the two lattices by dislocations (broken line) is energetically more favorable than by strain (energy $\overline{E}_\mathrm{D} < \overline{E}_\varepsilon$). (**b**) as a function of overlayer thickness; for thickness exceeding the critical thickness h_0 dislocations are energetically more favorable than strain (energy $\overline{E}_\mathrm{D} < \overline{E}_\varepsilon$)

Fig. 3.17 Critical thickness h_0 versus lattice mismatch $(b-a)/a$ for $\mathrm{Si}_{1-x}\mathrm{Ge}_x$ overlayers on a Si substrate. The experimental data originate from overlayers deposited by MBE (Sect. 2.4) at different substrate temperatures [3.14]

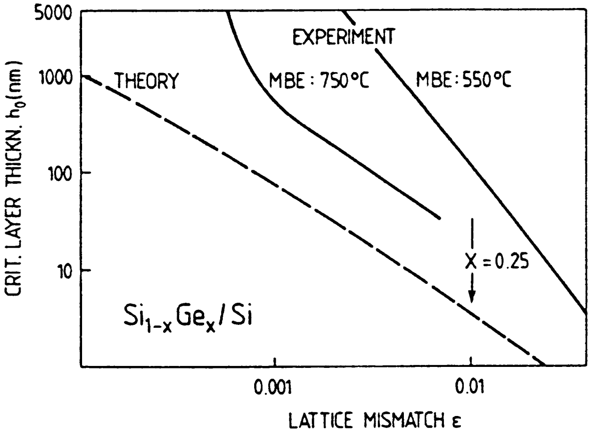

increases with growing layer thickness and for thicker layers the formation of dislocations eventually becomes favorable.

According to Fig. 3.16 the critical layer thickness is also a function of the lattice mismatch between two materials. Theoretical values are compared with experimental ones for the system of a mixed $\mathrm{Si}_{1-x}\mathrm{Ge}_x$ overlayer on Si in Fig. 3.17 [3.14]. Depending on the preparation method, in particular the substrate temperature, the theoretically expected curve is considerably lower than the experimental ones. This demonstrates that kinetic limitations, e.g. details of the nucleation process, are also important for the type of mismatch relaxation.

3.5 Nucleation and Growth of Thin Films

3.5.1 Modes of Film Growth

Of major importance in modern technology are solid interfaces between thin films and solid substrates, and, in particular, epitaxial films that have been grown on crystalline material by one of the methods MBE or MOMBE discussed in Sects. 2.4 and 2.5. Thus it will be useful to look, in a little more detail, at the process of film growth and the underlying principles which determine the structure and morphology of a particular film and the related interface to its substrate [3.15].

The individual atomic processes which determine film growth in its initial stages are illustrated in Fig. 3.18. Condensation of new material from the gas phase (molecular beam or gas phase ambient) is described by an impinging rate (number of particles per cm^2 per second)

$$r = p(2\pi MkT_0)^{-1/2}, \tag{3.22}$$

where p is the vapor pressure, M the molecular weight of the particles, k Boltzmann's constant, and T_0 the source temperature. Once a particle has condensed from the vapor phase, it might immediately re-evaporate or it may diffuse along the

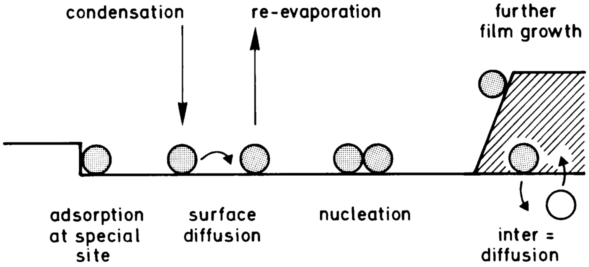

Fig. 3.18 Schematic representation of atomic processes involved in film growth on a solid substrate. Film atoms shown as dark circles, substrate atom as open circle

surface. This diffusion process might lead to adsorption, particularly at special sites like edges or other defects (Sect. 3.2), or the diffusing particle may re-evaporate. In all these processes, characteristic activation energies have to be overcome, i.e. the number of particles being able to participate in the particular process is given by an Arrhenius-type exponential law; the desorption rate, for example, is given by (also Sect. 10.5)

$$v \propto \exp(E_{\mathrm{des}}/kT), \tag{3.23}$$

where E_{des} is the activation energy for desorption. The corresponding activation energies for adsorption or diffusion depend on the atomic details of the process. Their origin will be discussed in more detail in connection with the theory of adsorption in Chap. 10. Besides adsorption at special defect sites and surface diffusion, nucleation of more than one adsorbed particle might occur, as might further film growth by addition of particles to an already formed island. How many particles are needed to form a new nucleus, which further grows into an island, is an interesting question, and one for which simple theoretical answers do exist. During film growth, interdiffusion is often an important process (Sect. 3.4). Substrate and film atoms hereby exchange places and the film substrate interface is smoothened. In order to obtain smooth film surfaces during growth, sufficiently high surface mobility of the diffusing species and therefore elevated temperatures are needed.

In thermodynamic equilibrium all processes proceed in two opposite directions at equal rates, as required by the principle of “detailed balance”. Thus, for example, surface processes such as condensation and re-evaporation, decay and formation of 2D clusters must obey detailed balance. Therefore, in equilibrium, there is no net growth of a film and so crystal growth must clearly be a non-equilibrium kinetic process.

The final macroscopic state of the system depends on the route taken through the various reaction paths indicated in Fig. 3.18. The state which is obtained is not necessarily the most stable one, since it is kinetically determined. In general, certain parts of the overall process may be kinetically forbidden, whereas others may be in local thermodynamic equilibrium. In this case equilibrium arguments may be applied locally even though the whole growth process is a non-equilibrium process. Due to this non-equilibrium nature of the process, a global theory of film growth requires a description in terms of rate equations (kinetic theory) for each of the processes depicted in Fig. 3.18 [3.16, 3.17]. Monte Carlo computer simulations have meanwhile been proven to be a powerful tool for such theoretical investigations.

Instead of following this more theoretical atomistic approach we will consider the process of film growth more phenomenologically. In general, three markedly different modes of film growth can be distinguished (Fig. 3.19). In the *layer-by-layer* growth mode (or Frank-van der Merve, FM) the interaction between substrate and layer atoms is stronger than that between neighboring layer atoms. Each new layer starts to grow only when the last one has been complete. The opposite case, in which the interaction between neighboring film atoms exceeds the overlayer substrate interaction, leads to *island growth* (or Vollmer-Weber, VW). In this case an island deposit always means a multilayer conglomerate of adsorbed atoms.

The *layer-plus-island* growth mode (or Stransky-Krastanov, SK) is an interesting intermediate case. After formation of one, or sometimes several complete monolayers, island formation occurs; 3D islands grow on top of the first full layer(s). Many factors might account for this mixed growth mode: A certain lattice mismatch (Sect. 3.4) between substrate and deposited film may not be able to be continued into the bulk of the epitaxial crystal. Alternatively, the symmetry or orientation of the overlayers with respect to substrate might be responsible for producing this growth mode.

A simple formal distinction between the conditions for the occurrence of the various growth modes can be made in terms of surface or interface energy γ, i.e. the characteristic free energy (per unit area) to create an additional piece of surface or interface energy. Since γ can also be interpreted as a force per unit length of boundary (see difference between surface energy and surface stress, Sect. 3.1), force equilibrium at a point where substrate and a 3D island of the deposited film touch (Fig. 3.20) can be expressed as

$$\gamma_S = \gamma_{S/F} + \gamma_F \cos\phi, \tag{3.24}$$

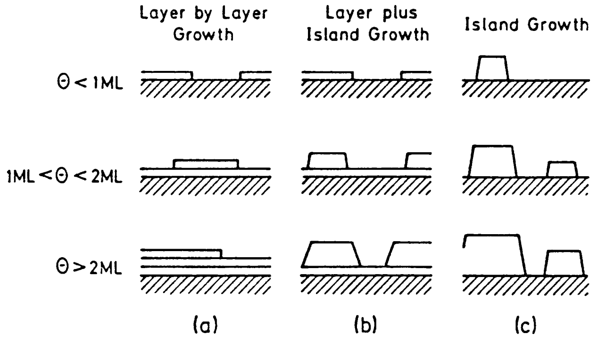

Fig. 3.19 a–c Schematic representation of the three important growth modes of a film for different coverage (θ) regimes (ML means monolayer). (**a**) Layer-by-layer growth (Frank-van der Merve, FM). (**b**) Layer-plus island growth (Stranski-Krastanov, SK). (**c**) Island growth (Vollmer-Weber, VW)

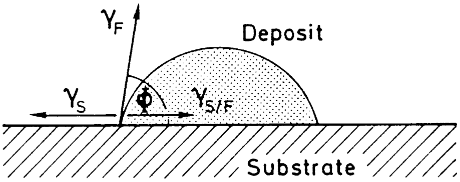

Fig. 3.20 Simplified picture of an island of a deposited film; γ_{S}, γ_{F} and $\gamma_{\text{S/F}}$ are the surface free energies between substrate and vacuum, between film and vacuum and between substrate and film, respectively

where γ_{S} is the surface free energy of the substrate vacuum interface, γ_{F} that of the film – vacuum, and $\gamma_{\text{S/F}}$ that of the substrate–film interface. Using (3.24) the two limiting growth modes, layer-by-layer (FM) and island (VW), can be distinguished by the angle ϕ, i.e.

$$\text{(i) layer growth}: \quad \phi = 0, \quad \gamma_{\text{S}} \geq \gamma_{\text{F}} + \gamma_{\text{S/F}}; \tag{3.25a}$$

$$\text{(ii) island growth}: \quad \phi > 0, \quad \gamma_{\text{S}} < \gamma_{\text{F}} + \gamma_{\text{S/F}}. \tag{3.25b}$$

The mixed Stranski-Krastanov growth mode (layer plus island) can easily be explained in this picture by assuming a lattice mismatch between deposited film and substrate. The lattice of the film tries to adjust to the substrate lattice, but at the expense of elastic deformation energy. The transition from layer to island growth occurs when the spatial extent of the elastic strain field exceeds the range of the adhesion forces within the deposited material.

The relations (3.25) are not complete if one considers the equilibrium condition for the whole system including the gas phase above the deposited film. Since the equilibrium is determined by a minimum of the Gibbs free enthalpy G, one has to take into account a contribution $\Delta G = n\Delta\mu$ (n is particle number), which is the change in (Gibbs) free energy when a particle is transferred from the gas phase into the condensed phase of the deposited film. If this transfer occurs exactly at the equilibrium vapor pressure $p_0(T)$, then no energy is needed because of the equilibrium condition $\mu_{\text{solid}} p_0(T) = \mu_{\text{vapor}}(p_0, T)$. If however the particle changes over from vapor to solid at a pressure p, a free enthalpy change (see any thermodynamics textbook on compression of an ideal gas)

$$\Delta G = n\Delta\mu = nkT \ln(p/p_0) \tag{3.26}$$

is involved. The ratio $\zeta = p/p_0$ is called the degree of *supersaturation*; as is easily seen from (3.26), ζ is one of the "driving forces" for the formation of a thin film deposited from an ambient vapor phase. Taking this vapor phase into account, the conditions for layer or island growth (3.26) have to be supplemented in the following way (C is a constant):

$$\text{(i) layer growth}: \quad \gamma_{\text{S}} \geq \gamma_{\text{F}} + \gamma_{\text{S/F}} + CkT \ln(p_0/p), \tag{3.27a}$$

$$\text{(ii) island growth}: \quad \gamma_{\text{S}} < \gamma_{\text{F}} + \gamma_{\text{S/F}} + CkT \ln(p_0/p). \tag{3.27b}$$

From (3.27) one sees that the growth mode of a certain material on a substrate is not a constant material parameter, but that the growth mode can be changed by varying the supersaturation conditions. With increasing supersaturation, layer-by-layer growth is favored. In vacuum deposition on solid substrates with low equilibrium vapor pressure p_0, supersaturation ζ might be high. In this case of vacuum deposition, the actual vapor pressure p is determined by the rate of impingement r, (3.22), in terms of the momentum transferred to the substrate per cm^2 per second. The supersaturation ζ might in this case, reach values of 10^{20} and more. Much lower ζ values are, of course, present in the epitaxy of III-V compounds (MBE, MOMBE, Sects. 2.4, 2.5) [3.17], where a substrate temperature of about 500°C causes relatively high equilibrium vapor pressures, at least for the group V component.

3.5.2 "Capillary Model" of Nucleation

A simple, but intuitively very appealing theoretical approach was proposed by Bauer [3.18] to describe island (3D cluster) and layer-by-layer (2D cluster) growth of nuclei on an ideal, defect-free, substrate surface [3.19]. Since this approach uses only the thermodynamically defined interface (surface) energies (Sect. 3.1) γ_S, γ_F, $\gamma_{S/F}$ of the substrate, of the film material and of the interface between substrate and film, respectively, it is called the *capillary theory of nucleation*. In this approach the total free enthalpy ΔG_{3D} or ΔG_{2D} for the formation of a 3D or a 2D nucleus, i.e. an aggregation of film atoms, on a substrate is considered as a function of the volume or the number of atoms constituting this nucleus. This free enthalpy is the sum of the contribution (3.26) gained upon condensation of the vapor and an energy cost for the formation of the new surfaces and interfaces of the nucleus (surface energies). As for every process a necessary condition for its occurrence is $\Delta G < 0$. This condition of decreasing free enthalpy then yields the limits for nucleation.

For *3D nucleation* (island growth) one obtains, with j as the number of atoms forming the nucleus,

$$\Delta G_{3D} = jkT \ln(p_0/p) + j^{2/3}X = -j\Delta\mu + j^{2/3}X. \tag{3.28}$$

The quantity X contains the contributions of the interface energy

$$X = \sum_k C_k \gamma_F^{(k)} + C_{S/F}(\gamma_{S/F} - \gamma_S). \tag{3.29}$$

$C_{S/F}$ is a simple geometrical constant which relates the basis area of the nucleus $A_{S/F}$ with the number of atoms according to $A_{S/F} = C_{S/F} j^{2/3}$. C_k relates $j^{2/3}$ to a part of the surface of the nucleus (adjacent to vacuum) having the surface energy $\gamma_F^{(k)}$. The outer surface of the nucleus, i.e. the part exposed to the vapor phase (or vacuum), is assumed in (3.29) to be composed of several patches of different crystallographic orientation with different surface energies $\gamma_F^{(k)}$.

For a simple, hemispherical nucleus (similar to that in Fig. 3.20) with radius r, (3.28) would read, with Ω as atomic volume of the film material,

$$\Delta G_{3D} = -\frac{1}{2}\frac{4}{3}\pi r^3 \Omega^{-1} \Delta\mu + 2\pi r^2 \gamma_F + \pi r^2 (\gamma_{S/F} - \gamma_S), \tag{3.30}$$

and $C_{S/F}$, for example, would amount to $\pi^{1/3}(3\Omega/2)^{2/3}$.

If we consider *2D nucleation*, i.e. the beginning of the growth of a layer on top of an ideally flat surface, the growth proceeds by incorporating new adsorbate atoms at the edges of the 2D cluster.

Corresponding to the surface energy there is a so-called *edge energy* γ_E per unit length, which describes the amount of energy necessary to position additional film atoms along the unit length of such an edge. The free enthalpy for 2D cluster growth, analogous to (3.36), is thus obtained as

$$\Delta G_{2D} = -j\Delta\mu + j(\gamma_F + \gamma_{S/F} - \gamma_S)\Omega^{2/3} + j^{1/2} Y. \tag{3.31}$$

where Ω is the atomic volume of the film material, and Y describes the effect of the adsorbate (film) atoms at the edges

$$Y = \sum_{\ell} C_\ell \gamma_E^{(\ell)}. \tag{3.32}$$

The sum over ℓ takes into account the fact that crystallographically different edge orientations ℓ may be associated with different edge energies γ_E^{ℓ}. C_ℓ are geometrical factors defined as the C_k and $C_{S/F}$ according to (3.29). On the assumption of a circular, planar nucleus of radius r formed by one atomic layer and with the film lattice constant a, the general equation (3.31) simplifies to

$$\Delta G_{2D} = -\pi r^2 a \Omega^{-1} \Delta\mu + \pi r^2 a \Omega^{-1/3} (\gamma_F + \gamma_{S/F} - \gamma_S) + 2\pi r \gamma_E. \tag{3.33}$$

In (3.28, 3.31) the last terms are positive and give rise to an increase of the free enthalpy with growing size of the nuclei; they form a nucleation barrier. The first terms ($\propto \Delta\mu$) being proportional to the logarithm of the supersaturation ζ are negative; they drive the nucleation process faster with increasing supersaturation and growing nucleus size. The superposition of the two effects generates a non-monotonic dependence of ΔG on the number of atoms j within the nucleus (Fig. 3.21); i.e., there exists a critical size of the nuclei both for 3D and for 2D nucleation, for which the free enthalpy ΔG becomes a maximum. If the nucleus reaches this critical size with a number of atoms j_{cr}, the cluster tends to grow rather than to decay. Below this critical cluster size, the nucleus is not stable, it tends to decay because ΔG increases with growing size.

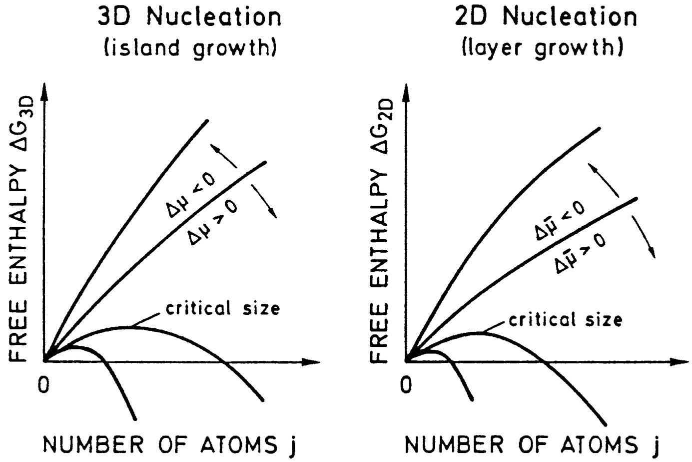

Fig. 3.21 Qualitative plots of free enthalpy changes ΔG_{3D} and ΔG_{2D} for 3D (island growth) and 2D (layer growth) film growth versus number of atoms j, forming the 3D or 2D clusters, respectively. The terms $\Delta\mu$ and $\Delta\bar{\mu}$ describe the dependence on the state of supersaturation

The *critical cluster sizes*, i.e. the critical number of atoms, j_{cr}, and the corresponding ΔG values are obtained by differentiating (3.28, 3.31):

$$\text{3D growth:} \quad \Delta G_{3D}(j_{\mathrm{cr}}) = \frac{4}{27}\frac{X^3}{\Delta\mu^2}, \quad j_{\mathrm{cr}} = \left(\frac{2X}{3\Delta\mu}\right)^3; \tag{3.34}$$

$$\text{2D growth:} \quad \Delta G_{2D}(j_{\mathrm{cr}}) = \frac{1}{4}\frac{Y}{\Delta\bar{\mu}}, \quad j_{\mathrm{cr}} = \left(\frac{Y}{2\Delta\bar{\mu}}\right)^2; \tag{3.35}$$

For layer-by-layer (2D) growth the second term in (3.31) is also negative because of the condition (3.25a); it thus augments supersaturation. In (3.35), therefore, $\Delta\bar{\mu}$ is an effective quantity

$$\Delta\bar{\mu} = \Delta\mu - (\gamma_{\mathrm{F}} - \gamma_{\mathrm{S/F}} - \gamma_{\mathrm{S}})\Omega^{2/3}, \tag{3.36}$$

which determines the critical 2D cluster size.

A comparison between (3.28 and 3.31) shows that, in principle, 3D cluster growth can only occur for $\Delta\mu > 0$, whereas 2D growth can also proceed for $\Delta\bar{\mu} > 0$. Because of the condition (3.25a) for layer-by-layer growth, the last term $(\gamma_{\mathrm{F}} + \gamma_{\mathrm{S/F}} - \gamma_{\mathrm{S}})$ in (3.36) is negative; 2D growth with $\Delta\bar{\mu} > 0$ can thus occur with $\Delta\mu \leq 0$, i.e. under conditions of subsaturation. In contrast, 3D growth requires supersaturation because of the requirement $\Delta\mu > 0$.

The rate J_{N} at which critical nuclei are formed is, of course, determined by the free enthalpies $\Delta G_{3D}(j_{\mathrm{cr}})$ and $\Delta G_{2D}(j_{\mathrm{cr}})$, respectively, for formation of a critical 3D or 2D nucleus (K is a constant):

$$J_{\mathrm{N}} = \mathrm{K}\exp\left[-\Delta G(j_{\mathrm{cr}})/kT\right]. \tag{3.37}$$

The nucleation rate J_N also determines the growth rate of a film. By comparing (3.26, 3.34, 3.35, 3.37), one sees that certain supersaturation and temperature conditions determine the critical nucleus size or atom number j_{cr}. This, in turn, also influences $\Delta G(j_{cr})$ and through (3.37) the formation rate of nuclei. The two extreme cases are the formation of many small nuclei or of a few large ones.

With increasing supersaturation ζ the number of atoms in a critical nucleus decreases both in the 3D and 2D cases according to (3.34, 3.35). Increasing the supersaturation thus causes smaller aggregation sizes and higher numbers of nuclei. In vacuum deposition, which often has high supersaturation at low substrate temperatures, the critical size of a nucleus might be very small – it may contain only a few atoms. In this limit then, the applicability of the classical theory with its macroscopically determined terms γ_F, γ_S, $\gamma_{S/F}$ is questionable.

Another limiting factor for the applicability of the classical capillary theory of nucleation must also be kept in mind: Only ideal, perfect substrate surfaces are taken into account. Special defect sites (point defects, edges, dislocations, etc.), which are extremely important for nucleation, are not considered. Nevertheless, capillary theory is helpful as a guide for predicting general trends in nucleation and film growth.

3.6 Film-Growth Studies: Experimental Methods and Some Results

The standard methods for studying the modes of film growth in situ are *Auger Electron Spectroscopy (AES)* and *X-ray Photoemission Spectroscopy (XPS)* in their simplest form of application (Panel XI and Sect. 6.3). Characteristic Auger transitions (usually differentiated spectra) or characteristic core-level emission lines (in XPS) of the substrate and of the adsorbate atoms are measured as a function of coverage. In both techniques the detected electrons originate from single atoms in the substrate or the adsorbate material. In AES they are released from a certain atomic level and carry an energy characteristic of a certain core-level transition (similar to characteristic X-ray lines): in XPS their energy corresponds to a characteristic core-level binding energy. But in both techniques, these electrons have to penetrate a certain amount of material, depending on the location of the emitting atom, before they can leave the crystal or the adsorbate overlayer. Thus, independent of the mode of excitation, the intensity I of the observed signal outside the film depends on the mean-free path of electrons of the particular energy and on the amount of matter which has to be penetrated. Because of the relatively "strong" interaction with matter (excitation of plasmons, etc.) the mean-free path λ of such electrons is in the order of a few Ångstroms, i.e. only electrons from the topmost atomic layers contribute to the detected AES or XPS signal. For the simplest case of layer by layer growth (FM) and assuming a simple continuum-type description the change of the AES or XPS line intensity dI is related to the change dh in film thickness by

$$\mathrm{d}I/I = -\mathrm{d}h/\lambda. \tag{3.38}$$

As in the case of absorption of electromagnetic radiation (then λ is the extinction length) one obtains an exponential decay of intensity due to the adsorbate thickness, i.e.,

$$I^{\mathrm{F}}/I^{\mathrm{F}}_{\infty} = 1 - \exp(-h/\lambda) = 1 - \exp(-\theta' d/\lambda). \tag{3.39}$$

where I^{F}_{∞} is the intensity measured on bulk film material, and θ' is the number of monolayers of the deposit (thickness of monolayer d). The intensity originating from substrate atoms after deposition of θ' monolayers of the film is then

$$I^{\mathrm{S}}/I^{0}_{\mathrm{S}} = \exp(-\theta' d/\lambda). \tag{3.40}$$

where I^{S}_{0} is the intensity of the substrate material without any deposited film.

Equations (3.39, 3.40) do not describe the detailed functional dependence. It is evident that during the growth of a monolayer, the signal intensity changes linearly with θ'. But the envelope of the curve being composed of several linear pieces is to a good approximation, given by an exponential function (Fig. 3.22). More extended theoretical approaches, taking into account the atomistic nature of the process, are able to reveal this fine structure [3.20]. It should further be emphasized that for non-normal emission, i.e. for detection of the AES or XPS electrons at an angle δ, the exponential extinction length in (3.39, 3.40) is not the free path λ, but must be corrected for the inclination of the surface to give $\lambda \cos \delta$.

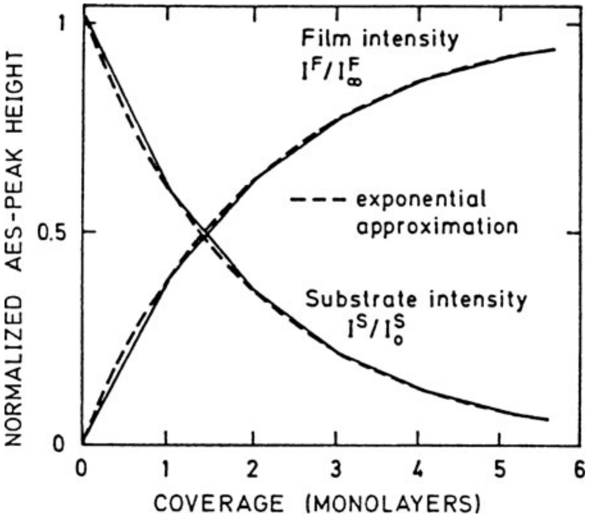

Fig. 3.22 Normalized Auger (AES) line intensities of substrate peak ($I^{\mathrm{S}}/I^{\mathrm{S}}_{0}$) and an adsorbate (overlayer) peak ($I^{\mathrm{F}}/I^{\mathrm{F}}_{\infty}$) as a function of coverage (in Mono-Layers, ML) for the layer-by-layer growth mode (Frank-van der Merve, FM). The solid curves are derived from a more detailed calculation [3.19]

It is evident that for island growth the intensity versus coverage dependence $I(\theta')$ will be very different from (3.39, 3.40). During film growth, large areas of the substrate remain free of deposit and the substrate signals are much less suppressed than in the case of layer-by-layer growth with complete overlayers. Only a slow increase and decrease of the film and of the substrate signal, respectively, is observed with the coverage θ' (Fig. 3.23c). Layer-plus-island (SK) growth is ideally characterised by a linear increase or decrease up to one or sometimes a few monolayers followed by a break point, after which the Auger or XPS amplitude increases or decreases (for film or substrate) only slowly. This regime corresponds to island formation on top of the first full monolayer(s). The gradient after the break point is dependent on the island density and shape and, of course, on the mean-free path of the particular electrons. Even though the three growth modes give qualitatively different AES and XPS patterns (Fig. 3.23), a clear distinction solely on the basis of AES or XPS results may be difficult. Similar AES and XPS dependences are expected, for example, for inhomogeneous film growth with interdiffusion and precipitations of substrate material in the film. Usually information from other measurements (SEM, LEED, RHEED, etc.) is needed to analyse the experimental data. Furthermore, model calculations, assuming, e.g., simple shaped islands (half spheres, circular flat disks, etc.), can help to quantify an observed $I(\theta')$ dependence.

An example of layer-by-layer (FM) growth is provided by the system InSb(110)-Sn [3.21]. Because of the chemical and electronic similarity of α-Sn to InSb, there is a nearly perfect lattice match of the semiconducting α-Sn modification (tetrahydrally sp^3 bonded) to InSb. As is seen by electron diffraction (LEED), α-Sn grows epitaxially on InSb(100), whereas on UHV-cleaved InSb(110) surfaces, no long-range order can be detected when Sn is deposited at room temperature [3.21]. But according to Fig. 3.24 the Auger intensity shows a clearly exponential behavior with coverage θ' over more than an order of magnitude, thus revealing the layer

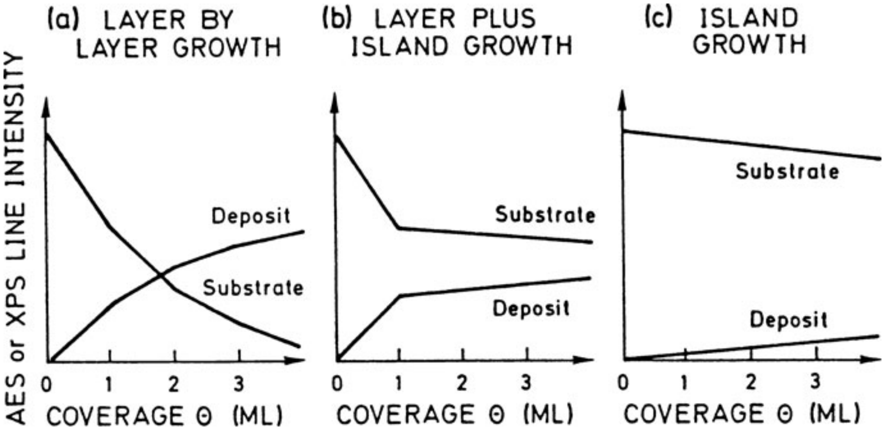

Fig. 3.23 Schematic Auger (AES) line intensities from deposit and substrate versus amount of deposited material (coverage θ) for (**a**) layer growth (FM), (**b**) layer-plus-island growth (SK), and (**c**) island growth (VW)

Fig. 3.24 Normalized Auger peak intensity of the In (410 eV) line versus coverage (in monolayers) for Sn deposited on cleaved InSb(110) surfaces. E_0 is the primary energy and λ the mean free path of 400 eV electrons in Sn [3.21]

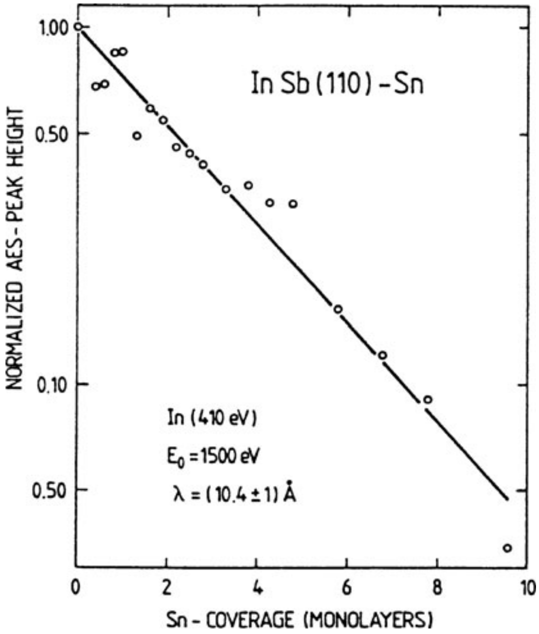

Fig. 3.25 Normalized Auger peak intensity of the Sn (437 eV) line versus coverage (in monolayers) for Sn deposited on cleaved InSb(110) surfaces. E_0 is the primary energy and λ the mean free path of 400 eV electrons in Sn [3.21]

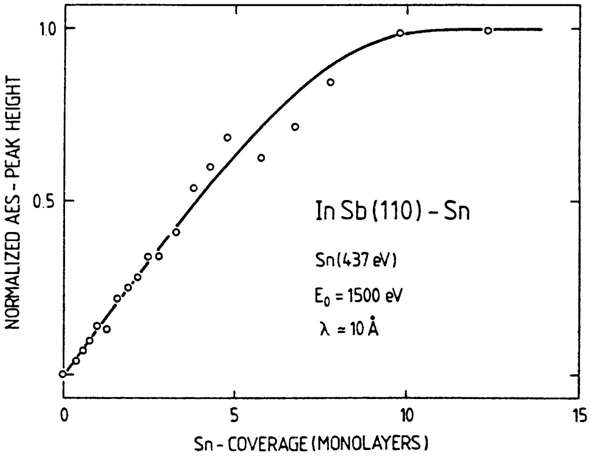

growth mode (FM). As expected from the mean-free path of about 10 Å (for 400 eV electrons) derived from the slope in Fig. 3.24, the AES signal intensity of the Sn film (Fig. 3.25) saturates near 10 monolayers. For thicker films the intensity does not increase further since the limiting factor is then the mean free path of the electrons rather than the amount of deposit.

On UHV-cleaved GaAs(110) surfaces the growth mode of Sn deposited at room temperature is different [3.22]. Figure 3.26 reveals a break in the substrate Ga emission line near a coverage of 1 to 2 monolayers, followed by a much slower decrease

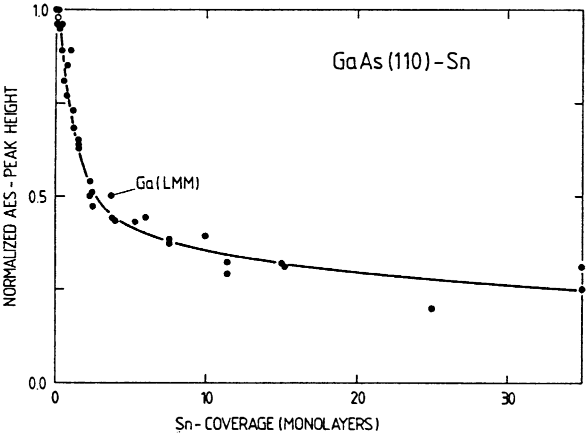

Fig. 3.26 Normalized Auger peak intensity of the Ga(LMM) line versus coverage (in monolayers) for Sn deposited on cleaved GaAs(110) surfaces [3.22]

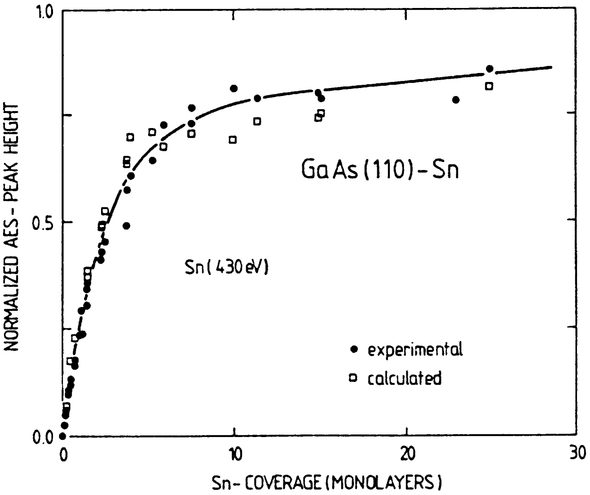

Fig. 3.27 Normalized Auger peak intensity of the Sn (430 eV) line versus coverage (in monolayers) for Sn deposited on cleaved GaAS(110) surfaces. As well as the experimental data points, results are also given of a theoretical model calculation (open symbol), where island formation on top of a closed β-Sn film of 3Å thickness is assumed [3.22]. The solid line is the best fit to the experimental data points

of the intensity. This behavior, as well as the corresponding intensity dependence of the Sn AES line (electron energy: 430 eV) is characteristic of Stranski-Krastanov (SK, layer plus island) growth. In Fig. 3.27 the full curve is obtained from a model calculation where the behavior of the AES intensity is attributed to the growth of a closed amorphous metallic β-Sn layer of about 3 Å thickness with hemispherical islands on top of this layer which grow in diameter with increasing film thickness. This model of SK growth is confirmed at higher coverages by scanning electron micrographs (Fig. 3.28), where at a nominal coverage of 38 monolayers of Sn an average island diameter of a few hundred Å is revealed.

Pure island (VW) growth is not found as often as the other two growth modes. The behavior of the characteristic Auger (or XPS) line intensities of deposit and substrate with coverage, as qualitatively shown in Fig. 3.23c, is sometimes difficult

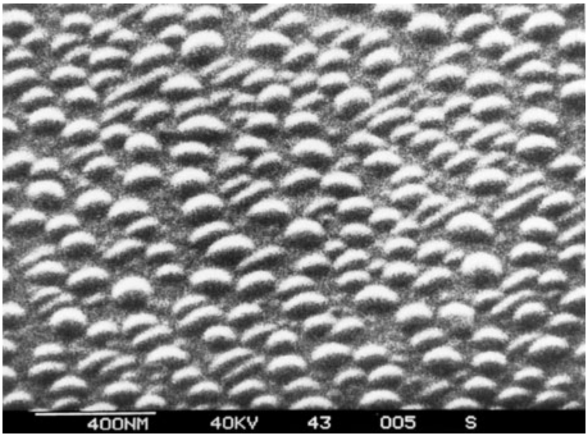

Fig. 3.28 Scanning electron micrograph of an Sn film (nominal coverage 38 monolayers) deposited on a cleaved GaAs surface [3.22]

to distinguish from the case of SK growth. Different experimental techniques have to be applied to discriminate between the two modes.

A number of experimental examples for the different types of film growth are listed in Table 3.3. The compilation does not explicitly take into account the type of interface formed: abrupt, more gradual, or with the formation of new chemical compounds as in the case of transition metals on Si (layer growth), where at the interface a new crystalline metallic compound, a Pt, Pd or Ni silicide, is formed, depending on the substrate temperature. On top of this silicide, layer-by-layer growth of the pure metal then occurs. It must be further emphasized, that the type of growth indicated in Table 3.3 is usually found only within certain substrate temperature ranges. Outside this range the growth behavior may be different.

An important class of experimental techniques for investigation of thin films grown under well-defined conditions is based on diffraction. *Electron diffraction*,

Table 3.3 Overview of some layer systems and their growth modes FM, SK, VW

Layer growth Frank-van der Merwe (FM)	Layer plus island growth Stranski-Krastanov (SK)	Island growth Volmer-Weber (VW)
many metals on metals e.g., Pd/Au, Au/Pd, Ag/Au, Au/Ag, Pd/Ag, Pb/Ag, Pt/Au, Pt/Ag, Pt/Cu	some metals on metals, e.g., Pb/W, Au/Mo, Ag/W, rare gases on graphite	most metals on alkali halides most metals on MgO, MoS_2 graphite, glimmer
alkali halides on alkali halides	many metals on semiconductors, e.g.:	
III-V alloys on III-V alloys e.g., GaAlAs/GaAs, InAs/GaSb GaP/GaAsP, InGaAs/GaAs	Ag/Si, Ag/Ge Au/Si, Au/Ge Al/GaAs, Fe/GaAs, Sn/GaAs	
IV semiconductors on some III-V compounds, e.g., Ge/GaAs, Si/GaP, α-Sn/InSb transition metals on Si Pt/Si, Pd/Si, Ni/Si (silicides)	Au/GaAs, Ag/GaAs	

which includes both LEED and RHEED (Panel VIII: Chap. 4), yields information about the crystallographic order of the deposit. The information, however, is limited by the finite coherence length of the electron beam. Only ordering over a range of a few hundred Angstroms contributes to the sharpness of the diffraction pattern. The observation of sharp LEED spots, therefore, indicates a well ordered crystal lattice only over such distances. Well developed Bragg spots do not necessarily indicate long-range crystallographic order. RHEED, in contrast to LEED, also gives information about the growth mode of the film. A flat surface, i.e. layer by layer growth means that the third Laue equation imposes no restriction; 2D elastic scattering usually gives rise to sharp diffraction stripes (Panel VIII: Chap. 4). The occurrence of 3D island growth brings the third Laue equation into play and spots rather than stripes are observed in the RHEED pattern.

Besides these diffraction techniques, which yield essentially a Fourier transform of the real-space structure, there are other techniques important in the study of film growth, that give real space images. *Scanning electron microscopy* (SEM [3.23], Panel V: Chap. 3) can provide a direct image of the film morphology (Fig. 3.28) down to dimensions of 10 Å in favorable cases. This lateral resolution in SEM is essentially determined by the diameter of the electron beam. SEM is usually performed ex situ, i.e. films prepared under UHV conditions have to be transferred through the atmosphere into the microscope. This might give rise to contamination-induced changes of the film structure, in particular in the low-coverage range. Only in special cases is SEM equipment available with UHV conditions and transfer units from the preparation chamber. It should also be noted that the SEM picture is produced by secondary electrons, whose emission intensity is not only affected by geometrical factors such as the type of surface, inclination to the primary beam, etc., but also by electronic properties of the surface such as work function and surface-state density, etc. Some of the intensity contrast in the image might therefore not be related to geometrical inhomogeneities but to electronically inhomogeneous areas. In particular, isolated islands of overlayer atoms should not be confused with patches of varying work function on the surface of a geometrically flat film.

Another direct imaging technique for the study of thin films is *scanning tunneling microscopy* (STM [3.24], Panel VI: Chap. 3). In this, the electron tunneling current between a metal tip of atomic dimensions and the film surface is measured as a function of lateral position of the tip. Scanning the tip over the surface yields a "real-space" image of the film surface. Even though it is actually an outer electron density contour that is probed rather than a geometrical surface, this type of surface imaging resembles a real "sensing" comparable to macroscopically drawing a pencil over a rough surface. Electronically processed two-dimensional scanning images or line scans can give a clear impression of the roughness and general morphology of a film surface right down to atomic dimensions (Fig. 3.29). The spatial resolution both laterally, i.e. parallel to the surface, and vertically, i.e., normal to the surface, is in the range of Ångstroms.

Direct imaging is, of course, also performed in *transmission electron microscopy* (TEM) [3.26]. Because of the limited penetration depth of electrons through solid

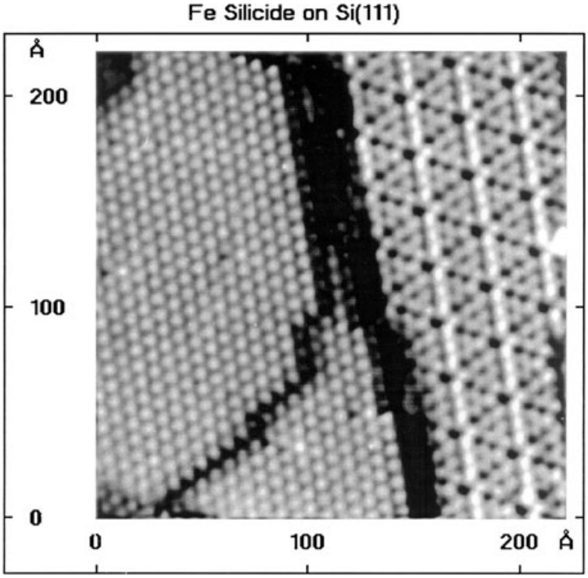

Fig. 3.29 Scanning Tunneling Microscope (STM) image of a Si(111)-(7 × 7) surface (superstructure seen in the right-hand part) covered with a $FeSi_2$ layer (left-hand part). Within the $FeSi_2$ layer a step is evident. The data were taken with a tunnel current of 1 μA and a tip voltage of 1.8 V; i.e. the filled Si states are seen [3.25]

material, conventional TEMs with acceleration voltages below 200 keV allow the analysis of samples having a maximum thickness of about 1 μm. Using high voltage instruments (acceleration voltages up to 3 MeV) thicker samples can be investigated. TEM can be used in a variety of ways to study thin films and overlayers. In the classical experiments on island growth and 3D nucleation, metal is deposited by evaporation onto alkali halide surfaces prepared by cleavage in UHV. Subsequently, the metal film consisting of more or less coalescent islands (VW growth mode) is fixed by a deposited carbon film. Outside the UHV chamber the alkali halide substrate is dissolved from the carbon film by water treatment and the films with the embedded metal clusters and islands are analysed with respect to shape, distribution, and number of islands by conventional TEM techniques. In particular, nucleation rates of metals versus temperature T (or versus $1/T$) have been studied for alkali-halide surfaces. For Au on KCl(100) surfaces (Fig. 3.30) an exponential dependence of the nucleation rate J_N on $1/T$, as predicted by (3.37), was found [3.16]. Additionally the nucleation rate depends quadratically on the adsorption rate u the density of adsorbed atoms is $u\tau_a$ (where τ_a is the adsorption time). From plots such as Fig. 3.30, the free enthalpy of cluster formation $\Delta G(j_{cr})$ (3.37) can be derived.

More refined preparation techniques are needed to study the crystallographic quality (dislocations, etc.) of thin films and the degree of perfection of heterointerfaces in TEM. The film must be imaged in a plane normal to the film–substrate interface. The sample therefore has to be cut normal to the interface, and thin slices have to be prepared by chemical etching and ion milling. Local thinning has to proceed down to dimensions of 10 to 100 nm, such that the electron beam can be transmitted. With conventional resolution, dislocations in the film can be

Fig. 3.30 Nucleation rate J_N divided by square of adsorption rate u for Au nuclei on a KCl surface, plotted versus reciprocal substrate temperature [3.16]

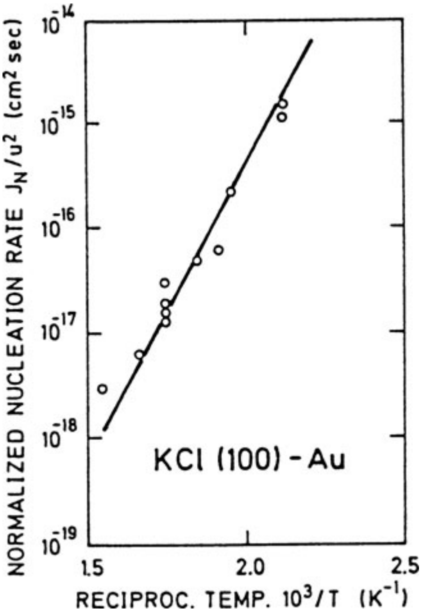

studied and their number and density can be evaluated (Fig. 3.31). For this purpose the sample is oriented in the electron beam slightly off from the Bragg condition. The strain field surrounding a dislocation causes the Bragg condition to be fulfilled locally, and part of the incoming beam is diffracted out of the transmitted beam. Part of the strain field of the dislocation then appears as a bright structure in a dark field or dark in a bright field image. In high-resolution TEM even the atomic structure of an interface can be resolved (Fig. 3.32). It must be emphasized, however, that the contrast seen in such a high-resolution electron micrograph is not directly related to single atoms. Rows of atoms are imaged and an involved theoretical analysis (taking into account details of the electron scattering process) is necessary for a detailed

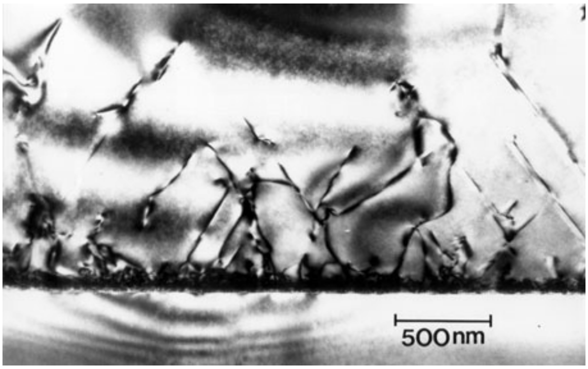

Fig. 3.31 Transmission Electron Micrograph (TEM) of dislocations in an epitaxial (110)GaAs overlayer on a Si substrate [3.27]

Fig. 3.32 High-resolution TEM of an AlAs/GaAs double heterostructure. The dark and bright points are correlated with single rows of atoms [3.28]

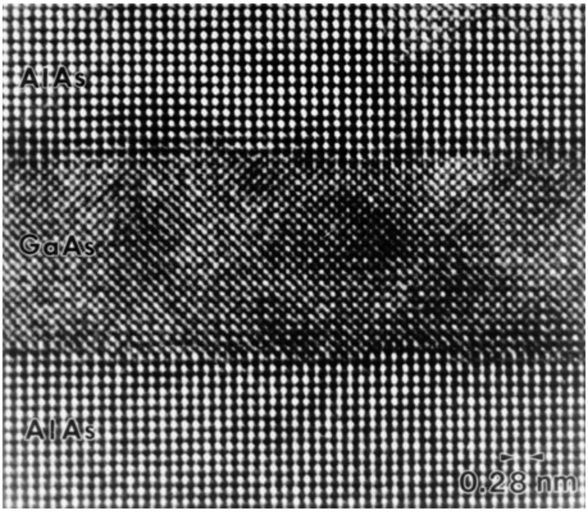

interpretation of the dark and light spots in terms of atomic positions. Nevertheless, information about the quality of an interface, in particular about the orientation of lattice planes, etc., can be obtained by simple inspection.

Optical methods are also successfully applied to the study of thin films. The *Raman effect* [3.29, 3.30] (inelastic scattering of photons in the visible or UV spectral range) allows one to study the vibrational properties of thin films, which can yield interesting information about their morphology. An example is exhibited in Fig. 3.33. Sb overlayers have been deposited under UHV conditions on cleaved

Fig. 3.33 a,b Raman spectra of Sb overlayers on lightly n-doped GaAs(110) surfaces prepared by cleavage in UHV; excitation by laser lines at 406.7 nm and 530.9 nm. The substrate temperatures T during deposition were 90 K (**a**) and 300 K (**b**). The coverage θ is given in MonoLayers (ML) on the spectra [3.30]

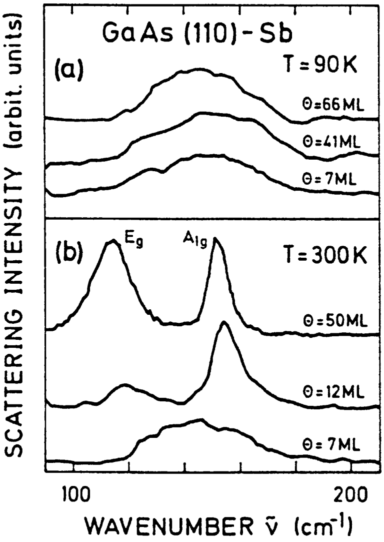

GaAs(110) surfaces. From LEED and other techniques it is known that the first monolayer of Sb is well ordered with a (2 × 1) superstructure. Additional deposition of Sb on top of this first layer leads to thicker layers which do not show any crystallographic order in LEED. Characteristic phonons of Sb, as measured by the Raman effect, reveal more details about these thicker overlayers. Because of its rhombohedric (D_{3d}) symmetry, crystalline Sb has two Raman active phonon modes at the Γ point, one of type A_{1g} and the other a twofold degenerate E_g mode. The corresponding lines are seen for thicker layers ($\theta' = 50\,\mathrm{ML}$, Fig. 3.33b) after deposition at 300 K. Since photons transfer only a negligible wave vector $\boldsymbol{q}$ in the scattering process, and since for a crystalline solid with 3D translational symmetry wavevector conservation applies, only phonons with a well-defined $\boldsymbol{q}$ vector near Γ contribute to the relatively sharp phonon lines (FWHM $\simeq 10\,\mathrm{cm}^{-1}$). Their sharpness, together with the lack of any long range order in LEED, indicates a polycrystalline morphology of the Sb layers deposited at 300 K and with thickness exceeding about 10 ML. For thinner layers ($\theta' < 10\,\mathrm{ML}$, Fig. 3.33b) a broad, smeared-out structure is seen. This clearly demonstrates that the Sb overlayers are amorphous. Due to the lack of translational symmetry in amorphous material, the wave vector is not conserved upon light scattering and phonons from all over the Brillouin zone contribute to give essentially an image of the phonon density (versus energy) rather than of single sharp phonon branches. Deposition at 90 K leads to amorphous Sb layers even in the high coverage regime as is seen from the featureless, broad spectral structure in Fig. 3.33a. It is obvious that phonon-line broadening in a Raman spectrum can thus be used to get information about the degree to which wave vector conservation is violated due to finite crystallite size in a polycrystalline layer. Not only can the amorphous state be distinguished from a polycrystalline morphology, but the crystallite size can also be estimated. According to a number of experimental data, sharp phonon lines, as expected for large bulk crystals, are observed in Raman scattering for crystallites with diameters exceeding 100 to 150 Å.

Among the various optical measurements on thin films, *ellipsometry* (Panel XII: Chap. 7), in particular when used as a spectroscopy, is of considerable importance. In ellipsometry, the optical reflectivity of the film–substrate system is determined by measuring the change of the polarisation state of light upon reflection [3.31]. The reflectivity measurement is thus reduced to a measurement of angles (Panel XII), which yields extremely high surface sensitivity ($< 10^{-1}$ monolayers of an adsorbate) in comparison with conventional intensity measurements. The underlying reason for this surface sensitivity is the high accuracy by which the angle of polarisation can be measured in contrast to a reflection intensity measurement, which is inherently less accurate. The change of the state of polarisation upon reflection can be expressed in terms of the ratio of the two complex reflection coefficients $r_\parallel$ and $r_\perp$ for light polarized parallel and perpendicular to the plane of incidence (containing incident and reflected beam), r being the ratio of reflected and incident electric field strength. The complex quantity

$$\rho = r_\parallel / r_\perp = \tan\psi \exp(\mathrm{i}\Delta) \tag{3.41}$$

defines the two ellipsometric angles Δ and ψ that are measured in ellipsometry (Panel XII: Chap. 7). Δ and ψ completely determine the two optical constants n (refractive index) and κ (absorption coefficient) or $\mathrm{Re}\{\varepsilon\}$ and $\mathrm{Im}\{\varepsilon\}$ (dielectric functions) of an isotropic reflecting medium (semi-infinite halfspace). For film growth and adsorption studies in interface physics one usually measures changes $\delta\Delta$ and $\delta\psi$ in the values of Δ and ψ for the clean surface and for the film (or adsorbate) covered surface. Most interesting are in situ measurements under UHV conditions. Even in the simplest *one-layer model* five parameters, the dielectric functions of substrate ($\mathrm{Re}\{\varepsilon_s\}$, $\mathrm{Im}\{\varepsilon_s\}$) and film ($\mathrm{Re}\{\varepsilon_f\}$, $\mathrm{Im}\{\varepsilon_f\}$) and the film thickness d determine $\delta\Delta$ and $\delta\psi$ [3.31]. The commonly applied analysis of experimental spectra $\delta\Delta(\hbar\omega)$ and $\delta\psi(\hbar\omega)$ is based on known substrate optical constants ($\mathrm{Re}\{\varepsilon_s\}$, $\mathrm{Im}\{\varepsilon_s\}$) and fitting spectra calculated with assumed film optical constants to the experimental spectra. The approximate film thickness is obtained from a measurement of the total amount of deposited film material by means of a quartz balance. The optimum fit then yields the dielectric functions $\mathrm{Re}\{\varepsilon_f\}$, $\mathrm{Im}\{\varepsilon_f\}$ of the film. Ellipsometric spectroscopy, when used in film growth studies, is most frequently applied to the determination of film optical constants and thus yielding integral information about the chemical and structural nature of a film and its global electronic structure. Figure 3.34 shows, as an example, results [3.32] obtained on the same InSb(110)-Sn system, as discussed in connection with Figs. 3.24 and 3.25. For coverages below about 500 Å ($\approx$ 200 monolayers of Sn) the dielectric functions (Fig. 3.34a) with their spectral structure due to electronic interband transitions are characteristic of semiconducting (gray)

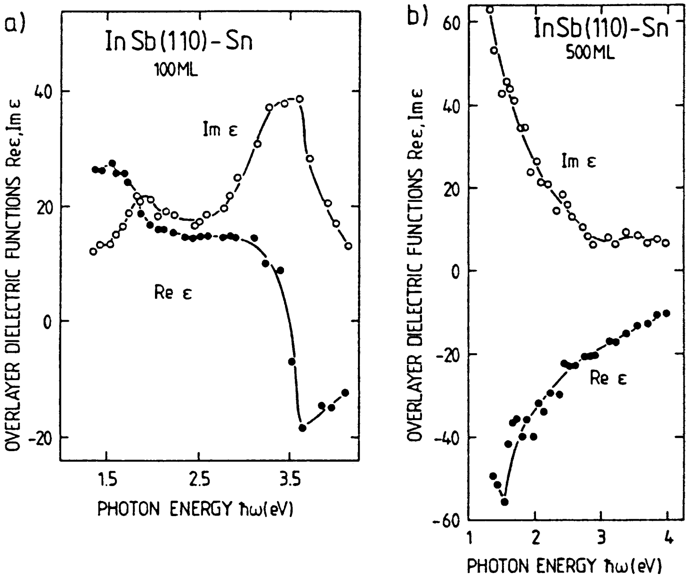

Fig. 3.34 a,b Real and imaginary parts of the dielectric function ε_f of Sn overlayers deposited in UHV on clean cleaved InSb(110) surfaces. The ellipsometric measurements were performed in situ on overlayers with differing thickness (coverage in MonoLayers, ML) [3.32]

α-Sn, whereas for thicker Sn layers (> 500 Å) the well-known behavior of the dielectric response of a quasi-free electron gas is observed (Fig. 3.34b). Sn layers at higher coverage are thus deposited as metallic β-Sn. Simultaneous LEED studies show that neither the α-Sn nor the β-Sn modification possesses long-range order; the deposit is in both cases polycrystalline. The stabilization of the tetrahedrally bonded α-Sn species even at room temperature (usually it is stable only at low temperature) is obviously due to the isoelectronic nature of α-Sn and InSb.

In applied technology, ellipsometry using a single light wavelength is often employed to determine film thicknesses. In this case the optical constants of the substrate and of the film material must be known and only d is calculated via Fresnel's formulae from the measured $\delta\Delta$ and $\delta\psi$.

An important technique for studying thin films and interfaces between overlayers and substrates is *ion scattering* with medium and high-energy (Rutherford BackScattering, RBS). In Sects. 4.9–4.11 the method and the underlying physics are described in more detail. A whole variety of information can be extracted from RBS measurements. Energy analysis of the backscattered ions (primary energy between 5 keV and 5 MeV) can be used as a chemical surface analysis technique, i.e., to probe the chemical nature of a particular surface layer, or a segregation on top of it (Sect. 4.10, Fig. 4.10). Measurement of the angular distribution of the backscattered particles and of the scattering yield as a function of angle of incidence gives detailed information about (i) the crystallographic quality of an epitaxial film and (ii) relaxations, lattice mismatch and internal strain (Sect. 4.11, Figs. 4.35, 4.36). The concept on which these measurements rely is that of "shadowing and blocking" of ion beams in certain crystallographic directions (Sect. 4.11).

In conclusion, the study of film growth is an expanding field, both in fundamental and in applied research. Many experimental techniques are available, on the macroscopic level as well as with atomic resolution. A complete compilation is beyond the scope of the present book; the aim of this chapter was to give the reader a first impression and an overview of this wide field of research.

Panel V
Scanning Electron Microscopy (SEM) and Microprobe Techniques

Scanning techniques (see also Panel VI: Chap. 3) have the common feature that a certain physical quantity is measured with spatial resolution and recorded as a function of position on the surface. The local distribution of this quantity is obtained electronically and viewed on an optical display, usually a TV screen. Of prime importance for the characterization of microstructures on a scale down to 10 Å are Scanning Electron Microscopes (SEM) [V.1] and microprobes. In addition to simple imaging of surface topography (SEM), a local surface analysis in terms of chemical composition can also be performed by the scanning electron microprobe.

The basic principle of these techniques consists in scanning a focussed electron beam (primary energy typically 2–10 keV) over the surface under study and simultaneously detecting electrons emitted from the surface. The intensity of this emitted signal determines the brightness of the spot on a TV tube. The formation of a topographical image is due to local variations of the electron emissivity of the surface. The operation of a SEM is described in more detail in Fig. V.1. The scanned electron beam is produced in an electron microscope column. Electrons are emitted from a heated W or LaB_6 cathode (or field emission cathode) and are focussed by the Wehnelt cylinder and an anode aperture into a so-called *cross-over point*. The cross-over point is projected by a first magnetic lens onto a smaller image point, which is further reduced by a second magnetic lens onto the sample surface. This image on the sample is reduced by a factor of about 1000 with respect to the primary spot. The best SEM columns can achieve focussing on the sample surface into a spot of about 10 Å. This spot size is the essential factor determining the spatial resolution of the SEM. Magnetic lenses [V.2] are used since they are more effective for high electron energies than electrostatic lenses ($\boldsymbol{F} = e\boldsymbol{v} \times \boldsymbol{B}$); aberration errors are smaller, too. The x-y scan is usually performed by two magnetic coils arranged perpendicular to one another between the two magnetic lenses. The amplification of the SEM is produced simply by electronically varying the deflection angle of the scanning electron beam. A video tube is employed as optical display; its electron beam is scanned synchronously with the primary probing beam of the microscope column, i.e. both beams are controlled by the same scanning electronics and the amplification of the SEM is adjusted by a scaling factor introduced essentially by a resistance divider circuit. The intensity of the electrons emitted from the sample determines (through an amplifier) the intensity of the TV tube beam. Different detectors sensitive to

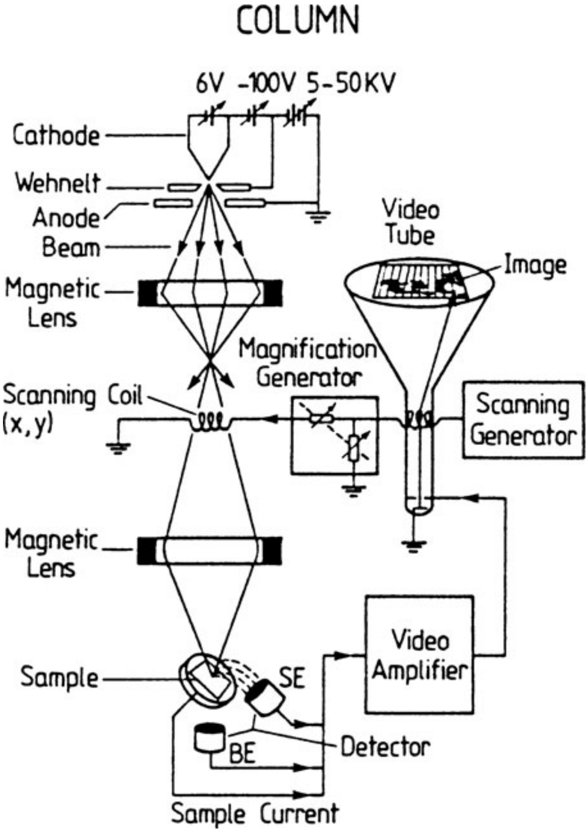

Fig. V.1 Schematic set-up of a scanning electron microscope or microprobe

various energy ranges of the emitted electrons can be used. A solid surface irradiated by an electron beam of energy E_0 emits electrons of various origin (Fig. V.2). Besides elastically backscattered electrons of energy E_0 (Region I), there is a regime of inelastically backscattered electrons (II), where the spectral structure stems from energy losses due to plasmon excitation and interband transitions (Chap. 4). These excitations are specific to every solid. A detector tuned to this energy range (BE in Fig. V.1) thus yields an image of the surface which is extremely sensitive to composition. A high contrast results from the material specificity of the emitted electrons. Because of the high degree of forward scattering (dielectric scattering with small wave-vector transfer $q_{\|}$, Sect. 4.6) in this loss regime, strong shadowing effects are observed for the threedimensional microstructures being imaged.

The spectrum of emitted electrons exhibits two other characteristic energy ranges, the next of these being a flat part between the above-mentioned loss regime and energies down to about 50 eV (Region III). With sufficient amplification (and detection usually in the differentiated mode $\mathrm{d}N/\mathrm{d}E$) the Auger emission lines characteristic for each chemical element can be detected in this energy range. The major

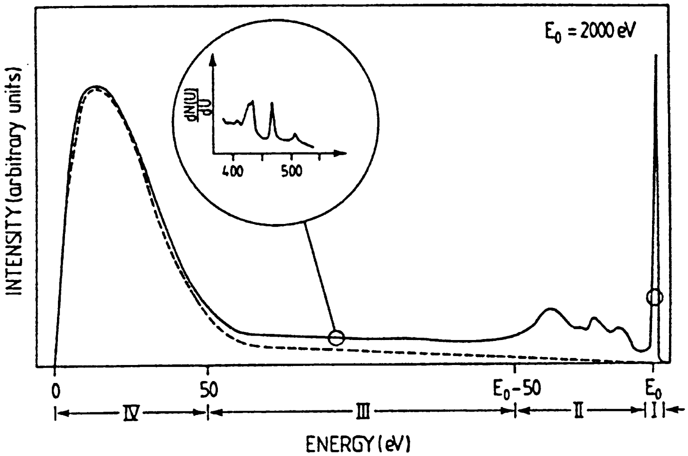

Fig. V.2 Qualitative large-scale overview of the energy distribution of electrons emitted from a surface which is irradiated by an electron beam of primary energy E_0. The true secondary-electron contribution is indicated by the dotted curve

part of the emission, the so-called *true secondary electrons*, form a strong and broad spectral band between 0 and 50 eV (Region IV), but extend as a weak tail up to E_0 The true secondary background originates from electrons that have undergone multiple scattering events (involving plasmons, interband transitions, etc.) on their way to the surface. Their spectral distribution and their intensity is thus not very specific to a particular material; nor is there a strong angular dependence of the true secondary emission as was the case for the inelastic losses in Region II. The detector SE in Fig. V.1 is tuned to record the lowenergy true secondary electrons and thus yields a different image of the surface from that obtained by detector BE. Due to the lack of forward scattering, less shadowing is observed. The contrast due to chemical composition is poorer but instead variations in surface roughness and work function are made visible. A topographical image similar to that from the detector SE, but with inverted contrast can be obtained by recording the total electric current from the sample, i.e. the total difference between the numbers of incident and emitted electrons (essentially the true secondaries).

Although, in principle, SEM pictures are not stereoscopic, good insight into the geometry of an object or a surface can be achieved by using different detectors and different irradiation geometries. However, one must expect some difficulties in the interpretation, since not only geometrical factors (inclination of planes, etc.) but also work-function variations and other electronic factors give rise to contrast changes. As an example of the application of SEM to the study of metal overlayers on semiconductors in microelectronics (Fig. V.3) shows golds contacts (bright structures) on a GaInAs/InP heterostructure. In the upper left part of the figure the GaInAs overlayer is seen, whereas the deeper laying InP substrate is exposed in the lower-right hand [V.4]. A further example is the SEM picture of a clean GaAs (110) surface (Fig. V.4a) which has been annealed in a separate UHV chamber up

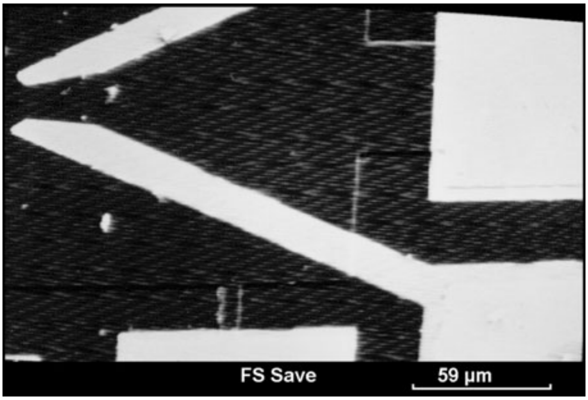

Fig. V.3 Scanning electron micrograph of gold contacts (bright structures) deposited on a GaInAs/InP heterostructure [V.4]

to temperatures around 1150 K. Segregation of material into islands is observed on the surface. The SEM pictures of Figs. V.3 and V.4a are obtained in a standard SEM under high vacuum conditions ($\approx 10^{-5}$ Pa), whereas the surfaces were prepared under UHV conditions in a separate chamber. Between preparation and the SEM study a transfer of the sample through air is necessary. This drawback of standard equipment has now been overcome by the development of SEMs that work under UHV conditions. These more advanced instruments can be connected via load lock chambers to other UHV equipment, such that, after preparation, SEM investigations of a surface or interface can be performed in situ.

In addition to measuring the secondary electron yield as a function of spatial position as in the SEM, other quantities can also be studied. The primary electron beam of a SEM also induces Auger processes (Panel III: Chap. 2) and the emission of X-rays [V.3]. Both Auger electrons and X-ray photons can be detected as a function of position by suitable detectors, Auger electrons by an electron analyzer (e.g., CMA; Panel II: Chap. 2) and photons, e.g., by an energy dispersive semiconductor photon-sensitive detector. Both the Auger signal and the X-ray emission are specific to a given element. Recording these quantities thus yields a spatially resolved picture of the distribution of chemical elements on a surface. The apparatus which is equipped with the appropriate instruments is sometimes called a *microprobe*. As an example Fig. V.4b shows the X-ray signals of the characteristic As line at 10.53 keV and the Ga line at 9.25 keV photon energy along a line scan intersecting the segregation in Fig. V.4a. The spatially resolved element analysis clearly exhibits the segregation of Ga islands on the GaAs surface after extended heating.

An example of a scanning Auger image is depicted in Fig. V.5. Sb has been evaporated on a UHV-cleaved GaAs(110) surface at a substrate temperature of about 300 K. After transfer through air the relative intensity of the Sb Auger line (integral over 454 and 462 V lines) $(I_{\mathrm{Sb}} - I_{\mathrm{back}})/I_{\mathrm{back}}$ was measured and the spatially resolved intensity distribution is displayed. The relatively homogeneous gray background indicates a quasi-uniform coverage of the GaAs surface with Sb. The dark spots are regions of lower cover age, i.e. they indicate deficiencies in the Sb overlayer. The bright spots (diameter ≈ 350 Å) originate from Sb islands which are formed

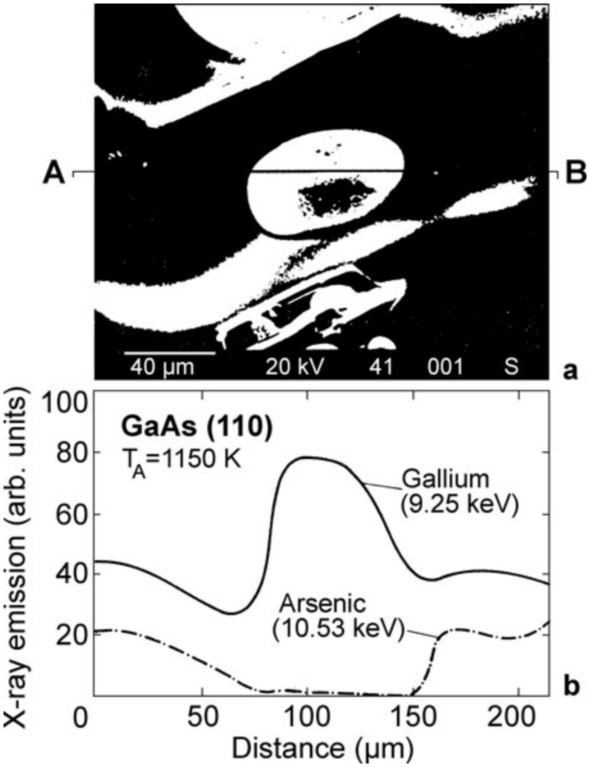

Fig. V.4 (**a**) Scanning electron micrograph of a GaAs(110) surface prepared by cleavage in UHV with subsequent annealing to 1150 K. The micrograph was taken ex situ after transfer through air. Segregation of substrate material into islands is visible. (**b**) X-ray emission signal for As (10.53 keV) and Ga (9.25 keV) measured along a line AB intersecting the segregation region in (**a**) [V.5]

on top of the more or less complete Sb underlayer. The AES image shows Stranski-Krastanov growth for the Sb overlayers on GaAs(110).

Although both the Auger intensity distribution and the characteristic X-ray emission pictures yield a local-element analysis of the surface, different depth information is obtained by the two probes. The absorption of X-ray photons by matter is weak, and thus the emitted photons originate from a depth range which is essentially determined by the penetration depth of the high-energy primary electrons. Depending on the material and the primary energy, the information depth for the X-ray probe is thus 0.1–10 µm. For the Auger probe, on the other hand, the information depth is given by the distance that the Auger electrons can travel without losing energy by scattering. This length is material dependent and is typically smaller by a factor of 10^2 to 10^4, as compared with the information depth of the X-ray probe. The characteristic differences between the information depth and the volume probed by the different techniques is shown schematically in Fig. V.6. Backscattered electrons and X-ray photons originate typically from a pearshaped zone below the surface,

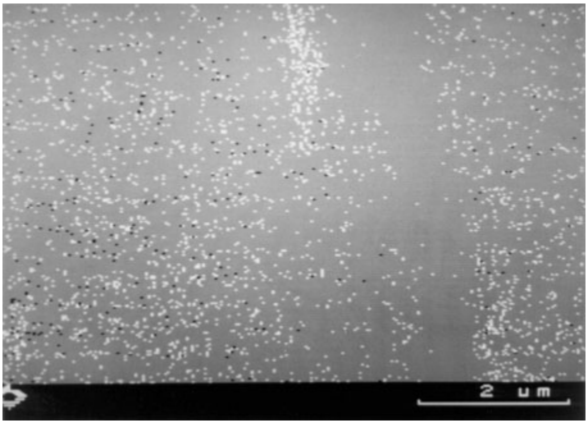

Fig. V.5 Scanning Auger electron micrograph of a GaAs(110) surface cleaved in UHV and covered with a nominal 5 monolayers of Sb. The Auger micrograph was recorded ex situ with a primary energy of 20 keV. The intensity distribution of the Sb lines (454 eV, 462 eV), i.e. $(I_{\mathrm{Sb}} - I_{\mathrm{back}})/I_{\mathrm{back}}$ displayed with a magnification of 10 000 [V.6]

whereas the low-energy secondary electrons and the Auger electrons carry information from the small, narrow neck of the "pear". The pear shape of the probed region arises from elastic and inelastic scattering of the high-energy primary electrons. It is evident from the distribution in Fig. V.6 that much better spatial resolution is obtained by the Auger probe ($\geq$ 10 nm as with SEM) than by using X-ray photons. On the other hand, the X-ray probe offers better depth analysis for the investigation of layer structures. For scanning Auger studies, UHV conditions are necessary because of the significant influence of surface contamination, whereas the X-ray probe can be used under conditions of poorer vacuum.

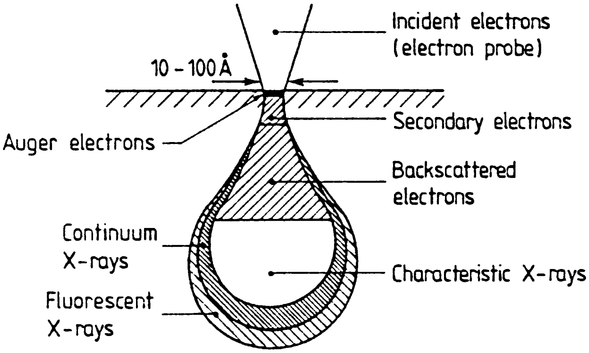

Fig. V.6 Schematic overview of the pear-shaped volume probed by different microprobe signals (electron and X-ray emission), when a primary electron beam is incident on a solid surface. Auger electrons originate from a depth of 5–20 Å, whereas the X-ray information depth is 0.1–10 µm with much less spatial resolution

References

V.1 L. Reimer: *Scanning Electron Microscopy*, Springer Ser. Opt. Sci. Vol. 45 (Springer, Berlin, Heidelberg, 1985)

V.2 P.W. Hawkes (ed.): *Magnetic Electron Lenses*, Topics Curr. Phys., Vol. 18 (Springer, Berlin, Heidelberg 1982)

V.3 B.K. Agarwal: *X-Ray Spectroscopy*, 2nd edn., Springer Ser. Opt. Sci. Vol. 15 (Springer, Berlin, Heidelberg, 1991)

V.4 H. Dederichs (ISI, Research Center Jülich): Private communication

V.5 W. Mockwa (Phys. Inst., RWTH Aachen): Private communication

V.6 H. Dederichs (ISI, Research Center Jülich): Private communication

Panel VI
Scanning Tunneling Microscopy (STM)

The Scanning Tunneling Microscope (STM), developed by Binning and Rohrer [VI.1], delivers pictures of a solid surface with atomic resolution. A direct realspace image of a surface is obtained by moving a tiny metal tip across the sample surface and recording the electron tunnel current between tip and sample as a function of position [VI.2]. In this sense the STM belongs to the wider class of scanning probes (Panel V: Chap. 3), in which a certain signal – in this case the tunnel current – is recorded and displayed electronically versus surface position.

Tunneling is a genuine quantum mechanical effect in which electrons from one conductor penetrate through a classically impenetrable potential barrier – in the present case the vacuum – into a second conductor [VI.3]. The phenomenon arises from the "leaking out" of the respective wave functions into the vacuum and their overlap within classically forbidden regions. This overlap is significant only over atomic-scale distances and the tunnel current I_T depends exponentially on the distance d between the two conductors, i.e. the tip and the sample surface. The now classic work of Fowler and Nordheim [VI.4] yields, as a first approximation, the expression

$$I_T \propto \frac{U}{d} \exp\left(-Kd\sqrt{\bar{\phi}}\right) \tag{VI.1}$$

where U is the applied voltage between the two electrodes, tip and sample, $\bar{\phi}$ their average work function ($\bar{\phi} \gg eU$), and K a constant with a value of about $1.025\,\text{Å}^{-1} \cdot (eV)^{-1/2}$ for a vacuum gap. I_T is easily measurable for distances d of several tens of Ångstroms and, in order to get interesting information about the surface, d must be controlled with a precision of 0.05–0.1 Å [VI.5].

To achieve a lateral resolution that allows imaging of individual atoms, the movement of the tiny metal tip across the surface under investigation must be controlled to within 1–2 Å. The high sensitivity of the instrument to the slightest corrugations of the surface electron density is due to the exponential dependence (VI.1) of I_T on d and $(\bar{\phi})^{1/2}$. Experimentally the stringent requirements for precise tip movement are satisfied by a two-step approach (Fig. VI.1): The sample is mounted on a piezoelectrically driven support called *louse*. This name derives from the fact that the stepwise movement of this support over distances of 100–1000 Å is achieved by three metallic legs carrying a piezoelectric plate. The legs act as electrostatic clamps which are successively attached to the metallic support plate by applying a voltage. When unbiased they move laterally by the action of the piezoelectric plate (voltage-induced tensions). This facility is employed for rough adjustment of the sample surface in front of the tip. The scanning of the tip across the surface is performed by means of a piezoelectric triple leg. Tip movement along three directions (x and y parallel, and z normal to the surface) with an accuracy of better than 1 Å are obtained by biasing the piezodrives by several tenths of a volt. Surface areas of typically $100 \times 100\,\text{Å}^2$ are scanned.

Recent, more easily operated STMs have been built with particular attention to a compact arrangement of sample, piezodrives and tip. A very compact construction (Fig. VI.1b), which is relatively insensitive to thermal drifts and mechanical

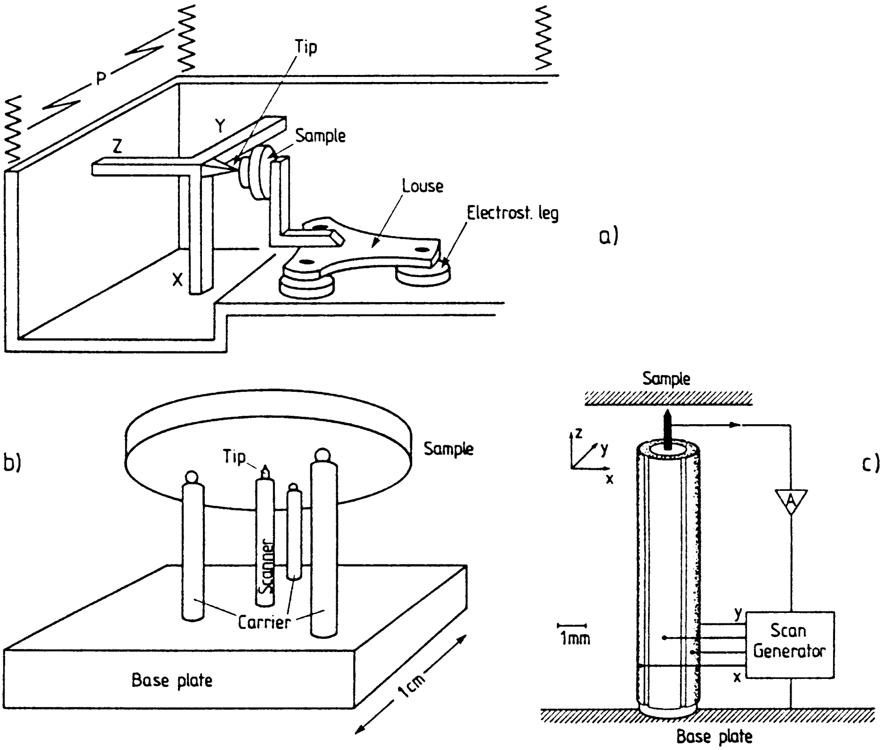

Fig. VI.1 (**a**) Schematic of the classic Scanning Tunneling Microscope (STM) [VI.1]. The metallic tip of the microscope is scanned over the surface of the sample with a piezoelectric tripod (x, y, z). The rough positioner or "louse", driven by controlled piezoelectric deformation of its main body, brings the sample within reach of the tripod. A vibration filter system P protects the instrument from external vibrations. (**b**) Schematic of the recent compact STM of Besocke [VI.6]. A large area sample, e.g. a semiconductor wafer, with its lower surface under study is carried by three piezoelectric actuators (carriers) which are used to produce microscopic shifts of the sample. A fourth piezoelectric rod (scanner) allows scanning of the metallic tip across the sample surface. (**c**) A function diagram of piezoelectric actuator element of part (**b**) equipped with tip and electronic connections for scanner operation. The carrier elements are identical in size and operation vibrations, uses three piezoelements as sample holder and distance control between tip and sample surface. A similarly constructed piezoelement in between carries the tip and is used as scanner. The piezoelements (Fig. VI.1c) are long rods with four separate metal electrodes. Biasing these electrodes causes bending of the rods. Actuating the x and y component of the three carriers simultaneously causes the sample to shift in the xy plane. Movements of the sample over macroscopic distances can be carried out by the simultaneous application of appropriate voltage pulses to all three carrier piezos. Adjustment and scanning of the tip are performed by suitably biasing the electrodes of the central scanner piezo.

Two major experimental difficulties had to be overcome in the development of the STM: suppression of mechanical vibrations of the whole equipment in its UHV chamber, and the preparation of a tip with atomic dimensions. Since the distance between tip and sample surface must be controlled down to an atomic radius, vibrational amplitudes must be damped down to less than an Ångstrom. In the original version of the STM, this vibrational damping was achieved by suspending the central part (Fig. VI.1a) on very soft springs and by the additional action of eddy currents induced in copper counter plates by powerful magnets. The development of more compact and simpler arrangements (Fig. VI.1b) is still continuing.

The tip is prepared from Ir or W wire (1 mm in diameter), which is grounded at one end to yield a radius of curvature below 1 μm. Chemical treatment follows, and the final shape of the tip end is obtained by exposing the tip in situ to electric fields of 10^8 V/cm for about ten minutes. The detailed mechanism of tip formation (adsorption of atoms or atomic migration) is not well understood at present. The method of preparation does not usually lead to very stable tips: Optimum resolution can only be achieved for a limited time and after a while the sharpening procedure has to be repeated.

According to (VI.1) the tunnel current depends both on the distance d between tip and surface, and on the work function. Changes of I_T might therefore be due to corrugation of the surface or to a locally varying work function. The two effects can be separated by an additional measurement of the slope of the tunnel characteristic during scanning. The normal measurement of surface corrugation is based on the assumption of constant $\overline{\phi}$; then keeping I_T constant, the voltage U_z on the z piezodrive is measured as a function of the voltages U_x, U_y on the x and z piezodrives (Fig. VI.1). The topography of the surface is obtained in terms of the corrugation function $z(x, y)$. I_T usually changes by an order of magnitude for changes in the distance d on the order of an Ångstrom. By keeping the tunnel current constant, changes in the work function are compensated by corresponding changes in d. Spurious structures in the surface morphology induced by work function changes can be identified by measuring $\overline{\phi}$ separately. This is done by recording the first derivate of I_T versus d using a modulation of the distance d, i.e. a modulation voltage U_z for the z-piezodrive ($U_z = U_z^0 + \tilde{U}_z$) and phase-sensitive detection (lock-in). According to (VI.1) the average work function $\overline{\phi}$ is easily obtained by

$$\overline{\phi} \simeq (\partial \ln I_\mathrm{T} / \partial d)^2. \tag{VI.2}$$

By recording both the signal I_T (or equivalently the compensating voltage U_z) and the derivative (VI.2) a distinction between topographical and work function changes becomes possible. Part of a commonly used electric circuit for this measuring procedure is shown schematically in Fig. VI.2. The essential parts are the feedback electronics for the z piezodrive and a circuit (including an xy ramp) controlling the x and y piezodrives. Figure VI.3 depicts a line scan (along x) over a cleaved Si(111) surface on which Au had been deposited [VI.7]. By comparison to the direct signal $I_T(d)$ and its derivative $[\propto (\bar{\phi})^{1/2}]$ the structures A and B are seen to be caused by workfunction inhomogeneities, i.e. Au islands.

A classic example of the use of the STM in surface structure analysis is the study of the Si(111)-(7 × 7) surface (Sect. 6.5). In the STM relief of the (7 × 7)

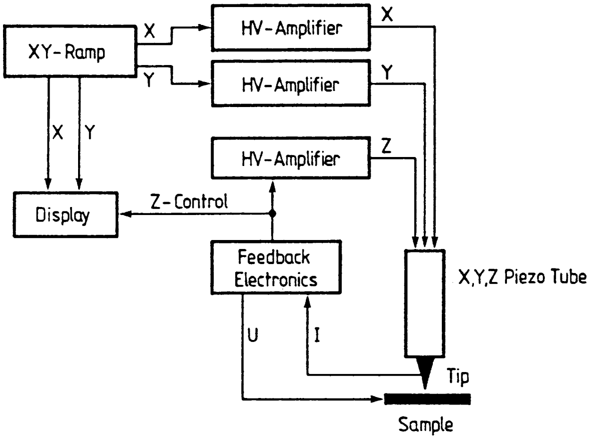

Fig. VI.2 (**a**) Main components of the electronics of a STM. The tunneling current through tip and sample controls the tip (z) movement via feedback electronics and a High Voltage (HV) amplifier. A digital ramp is used for the xy scan

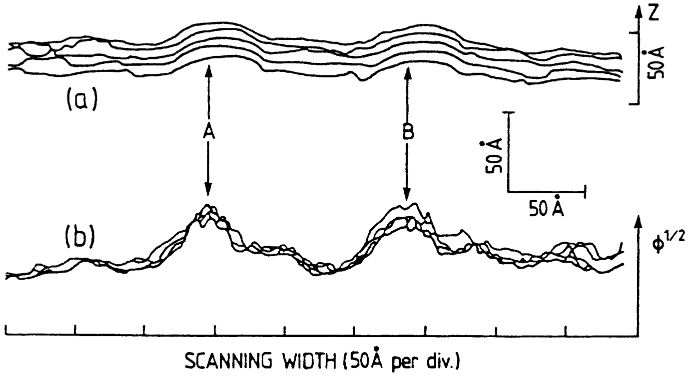

Fig. VI.3 a,b Line scans over a cleaved Si(111) surface on which Au has been deposited [VI.7]. (**a**) Direct measurement of the corrugation $z(x)$ and (**b**) derivative measurement $\partial \ln I_T/\partial d$ according to (VI.2), which yields information about the average workfunction reconstructed surface (Fig. VI.4) several complete unit cells are discernible on the basis of their deep corner minima [VI.8]. This realspace STM image of the Si(111)-(7 × 7) surface allowed to discard many of the existing structural models proposed for this surface. Although precise structural details cannot be established from Fig. VI.4 alone, there were many arguments in favor of a modified adatom model (Fig. 6.37), which finally led to a structure model for the (7 × 7) surface of Si(111) (Sect. 6.5). The STM results demonstrated, in particular, that the two halves of the unit mesh are not completely equivalent because of the slightly different heights of the minima and maxima (Fig. VI.4).

Since electron tunneling can occur from the metal tip to the semiconductor surface, or vice versa, depending on the direction of the bias, more information about the electronic structure of the surface can be obtained by studying the dependence of the STM signal on the sign and magnitude of the tip-sample voltage. This is qualitatively shown for opposite bias voltages in the tunnel-band schemes in Fig. VI.5. For positive bias in Fig. VI.5a, tunneling of electrons can only occur from occupied metal states into empty surface states or conduction-band

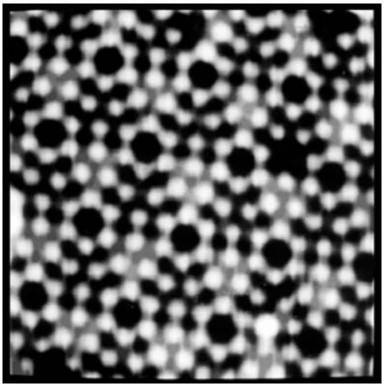

Fig. VI.4 STM relief of the (7 × 7) reconstructed Si(111) surface [VI.8]. The large unit mesh is discernible by the deep corner minima. The two halves of the unit mesh are not equivalent as evidenced by the different intensities of the minima and maxima

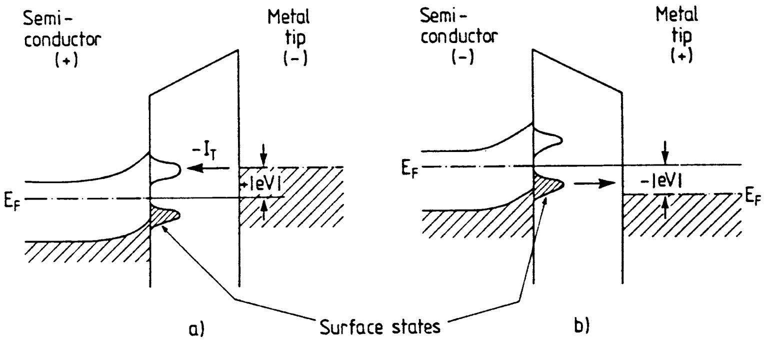

Fig. VI.5 a,b Electronic-band scheme of the semiconductor sample and the metal tip for two opposite values of bias voltage. (**a**) Tunneling of electrons from the metal tip into empty surface states in the sample, and (**b**) tunneling of electrons from occupied surface states in the sample into the metal tip states in the semiconductor. When the metal tip is positive with respect to the semiconductor surface (Fig. VI.5b) elastic tunneling of electrons from the metal into the semiconductor is not possible, only occupied states can be reached because of the Fermi-level position. The measured tunneling current I_T therefore originates from occupied surface or valence-band states in the semiconductor. Depending on the bias direction, therefore, occupied or empty states of the surface under investigation can be probed. By measuring the dependence of the current I_T on the applied voltage one can even obtain an image of the state distribution. An example of this kind of application is the STM study of the clean, cleaved Si(111)-(2 × 2) surface

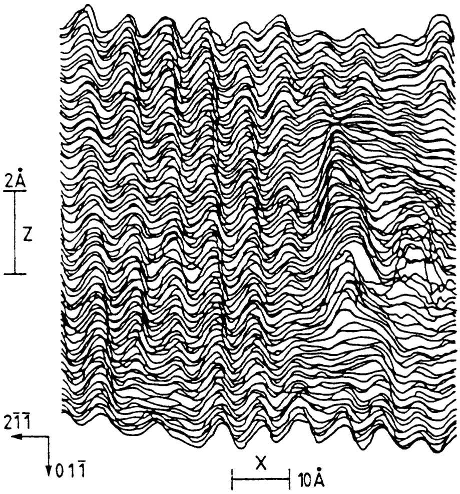

Fig. VI.6 STM relief of a cleaved Si(111) surface, measured at a sample voltage of +0.6 V. The image extends laterally over an area of 70 × 70 Å^2, with the vertical height given by the scale on the left-hand side of the figure. The (2 × 1) π-bonded chains are seen at the left thand side, and a disordered region is seen on the right [VI.9]

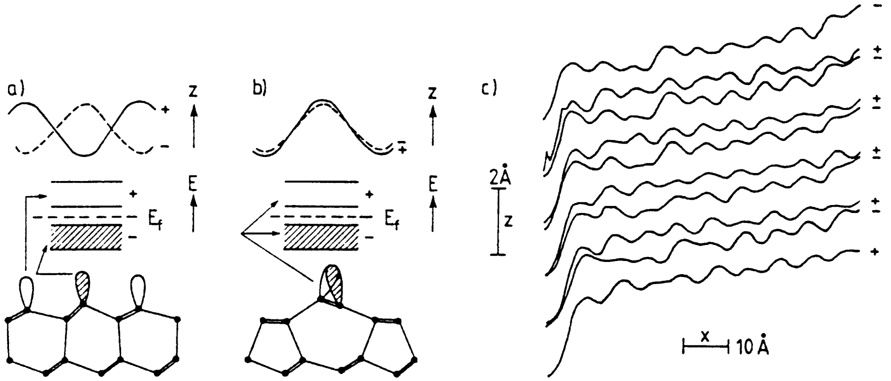

Fig. VI.7 Schematic view of the surface states on a (2 × 1) Si(111) surface for (**a**) the buckling model, and (**b**) the π-bonded chain model. Dangling bonds on the surface result in two bands of surface states above and below the Fermi level E_F. The corrugation $z(x)$ of these bands is measured separately by applying positive or negative voltages. (**c**) Experimentally determined line scans of the corrugation $z(x)$ measured with sample voltages +0.8 and −0.8 V. A monatomic step is seen at the left hand edge of the scans [VI.9]

(Sect. 6.5). A real space STM image [corrugation $z(x, y)$] (Fig. VI.6) depicts a linear corrugation along $(01\bar{1})$ with an amplitude of 0.54 Å and a raw spacing of about 6.9 Å [VI.9]. This spacing is not consistent with the surface atomic distances in a buckling model (Fig. VI.7a), but good agreement exists with the distance between two dangling bond chains in a π-bonded chain model (Sect. 6.5 and Fig. VI.7b). Further strong support for the π-bonded chain model is obtained from line scans of the tunnel current, i.e. the corrugation along $(2\overline{11})$, at opposite biases of $+0.8$ and -0.8 V. Although the occupied and empty surface states are probed separately in these two cases (Fig. VI.5), the maxima and minima of the corrugation occur at the same location, as is expected for the π-bonded chain model (Fig. VI.7b). The spatial phase shift that would be associated with the buckling model (Fig. VI.7a) is not observed. A measurement of the differentiated tunnel characteristics $\mathrm{d}I_\mathrm{T}/\mathrm{d}U$ (lock-in technique) as a function of positive and negative bias (Fig. VI.8a) then gives a qualitative picture of the spectral distribution of the occupied and empty surface states on Si(111)-(2 × 2). Good agreement with the distribution of π and π^* states predicted by the π-bonded chain model (Figs. VI.8b and 7.13) is found. The four dominant peaks are due to flat areas in the occupied bonding π and empty antibonding π^*-state bands.

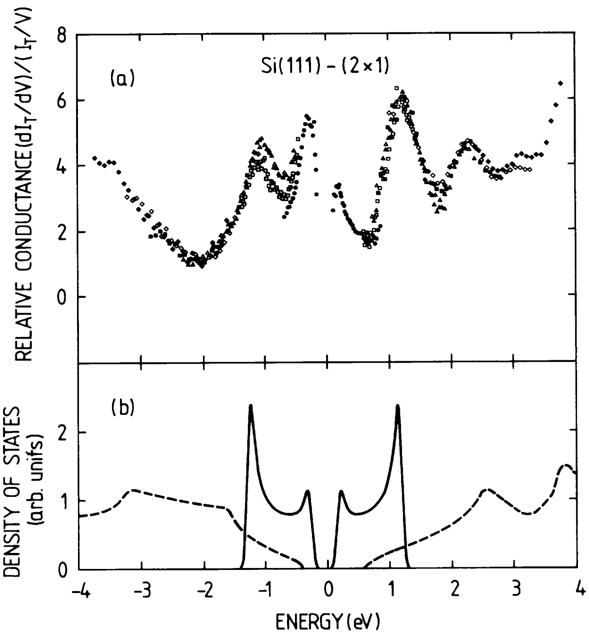

Fig. VI.8 (**a**) Ratio of differential to total tunneling conductance $(\mathrm{d}I_\mathrm{T}/\mathrm{d}U)/(I_\mathrm{T}/U)$ versus electron energy (relative to the Fermi energy E_F) measured by an STM on a cleaved Si(111)-(2 × 1) surface. The different symbols refer to different tip-sample separations [VI.10]. (**b**) Theoretical Density Of States (DOS) for the bulk valence and conduction bands of Si (dashed line) [VI.11], and the DOS from a one-dimensional tightbinding model of the π-bonded chains (solid line) [VI.10]

The present examples clearly demonstrate the great value of the STM in studies of the geometric and electronic structure of solid surfaces. The STM and a modification of this instrument, the Atomic Force Microscope (AFM) [VI.12, VI.13] has meanwhile also opened pathways to a new branch of science: *Nanotechnology*.

Nanotechnology, i.e., nanopositioning of atoms and molecules as well as controll of chemical processes on a nanometer (10^{-9} m) scale and nanoprecision machining has become possible by means of the STM and AFM. By scanning the tip of an STM while tip and substrate are in intimate contact, submicrometer-wide lines can be drawn by scratching the surface of a solid. By increasing the tip-sample interaction at a particular surface location indentations can be produced with an STM or AFM. Van Loenen et al. [VI.14] could produce holes of 2–10 nm diameter in a clean Si surface by means of an STM with a tungsten tip.

Even single atoms and molecules can be pulled and pushed on a substrate surface under UHV conditions at low temperature by an STM, as was first demonstrated by Eigler and Schweizer [VI.15]. After adsorption of Xe atoms on a Ni(110) surface single Xe atoms could be moved along the surface to form special figures or letters. For this purpose the tip is first positioned above the selected atom (pictured in the microscope mode). The interaction of the tip with this Xe atom, being essentially due to van der Waals forces, is then increased by approaching the tip toward the atom (Fig. VI.9). The tip is then moved laterally under constant-current conditions while carrying the Xe atom with it. Upon reaching the desired destination, the tip is finally withdrawn by decreasing the set-value of the tunnel current, leaving the Xe atom at the desired new position. By applying the sliding procedure to other adsorbed atoms as well (Fig. VI.9), overlayer structures can be fabricated atom by atom. For another example, see [VI.16].

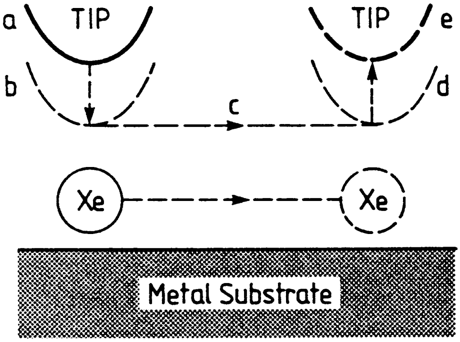

Fig. VI.9 Schematic illustration of sliding and positioning an atom across a surface by means of an STM. The tip is placed over the Xe atom (**a**), subsequently lowered to (**b**), where the atom-tip attractive force is sufficient to keep the atom beneath the tip. The tip is subsequently moved across the surface (**c**) to the desired destimation (**d**). Finally the tip is withdrawn to a position (**e**) where the atom-tip interaction is negligible. Thus the atom is releaved from the tip at a new location on the surface [VI.15]

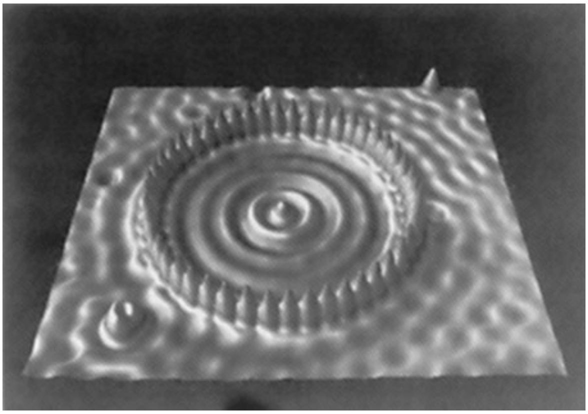

Fig. VI.10 Constant-tunneling-current STM image of a quantum corral consisting of 48 Fe atoms assembled in a ring on a Cu(111) surface at 4 K (imaging bias: 0.02 V). The ring with a diameter of 142.6 Å encloses a defect-free area of the surface. Inside of the corral a circular standing wave of electrons in *sp*-like surface states of the Cu(111) surface is visible. The bias parameters during the sliding process were 0.01 V and $5 \cdot 10^{-8}$ Å [VI.17]

A second type of moving an atom on a metal surface to a desired position is by simply pushing it by the STM tip. For this purpose the tip is lowered on top of the particular atom until strong interaction between the atom and the tip occurs. By moving the tip to the disered position the atom is dragged with it. The atom moving across the surface does not really break its chemical bond to the electron "sea" of the metal surface. Only the diffusion barrier being essentially 1/10 of the binding energy has to be surmounted by the tip adatom interaction.

A nice example of an artificial nanostructure prepared on a copper surface under UHV conditions by an STM is displayed in Fig. VI.10. Crommie et al. [VI.17] have assembled a so-called *quantum corral* by pushing and pulling 48 Fe atoms adsorbed at 4 K on a Cu(111) surface into a ring of radius 71.3 Å. Beside two seperate Fe atoms the circular corral consisting of the 48 Fe atoms is imaged by the STM after positioning them individually at the correct sites. Tunneling microscopy performed inside of the corral reveals a series of discrete resonances forming a kind of a ring-like standing wave. Since an STM probes electronic wave functions the standing wave within the corral must be due to electrons located at the Cu surface. As will be shown in Sect. 6.4, there are so-called *electronic surface states* at the Cu(111) surface which have free-electron character (Parabolic dispersion in Fig. 6.18). Electrons occupying these states are located at the very surface and their motion parallel to the Cu(111) surface is essentially that of free electrons. For these electrons the Fe atoms forming the circular corral are strong scattering centers, such that an electron is confined by the circular barrier. The spatial variation of the electronic density of states inside of the Fe ring can be described, even quantitatively, by the distribution of round-box eigenstates (Bessel functions) of electrons within *sp*-like Cu surface states near the Fermi level [VI.16].

References

VI.1 G. Binnig, H. Rohrer, Ch. Gerber, E. Weibel: Appl. Phys. Lett. **40**, 178 (1982); Phys. Rev. Lett. **50**, 120 (1983)

VI.2 H.-J. Güntherodt, R. Wiesendanger (eds.): *Scanning Tunneling Microscopy I*, 2nd edn., Springer Ser. Surf. Sci., Vol. 20 (Springer, Berlin, Heidelberg 1994)
R. Wiesendanger, H.-J. Güntherodt (eds.): *Scanning Tunneling Microscopy II, III*, 2nd edn., Springer Ser. Surf. Sci., Vols. 28, 29 (Springer, Berlin, Heidelberg 1995, 1996)
D.J. O'Connor, B.A. Sexton, R.St.C. Smart (eds.): *Surface Analysis Methods in Materials Science*, Springer Ser. Surf. Sci., Vol. 23 (Springer, Berlin, Heidelberg 1992) Chap. 10

VI.3 H. Ibach, H. Lüth: *Solid State Physics – An Introduction to Principles of Materials Science*, 4th edn. (Springer, Berlin, Heidelberg 2009)

VI.4 R.H. Fowler, L.W. Nordheim: Proc. Roy. Soc. A **119**, 173 (1928)

VI.5 P.K. Hansma, J. Tersoff: J. Appl. Phys. **61**, R2 (1987)

VI.6 K. Besocke: Surf. Sci. **181**, 145 (1987)

VI.7 G. Binnig, H. Rohrer, F. Salvan, Ch. Gerber, A. Baro: Surface Sci. **157**, L373 (1985)

VI.8 R. Butz (ISI, Research Center Jülich): Priv. commun.

VI.9 R.M. Feenstra, W.A. Thomson, A.P. Fein: Phys. Rev. Lett. **56**, 608 (1986)

VI.10 J.A. Stroscio, R.M. Feenstra, A.P. Fein: Phys. Rev. Lett. **57**, 2579 (1986)

VI.11 J.R. Chelikowsky, M.L. Cohen: Phys. Rev. B **10**, 5095 (1974)

VI.12 R. Wiesendanger: *Scanning Probe Microscopy and Spectroscopy* (Cambridge Univ. Press, Cambridge, UK 1994)

VI.13 C. Bai: *Scanning Tunneling Microscopy and Its Application*, 2nd. edn., Springer Ser. Surf. Sci., Vol. 32 (Springer, Berlin, Heidelberg 2000)

VI.14 E.J. Van Loenen, D. Djkkamp, A.J. Hoeven, J.M. Lenssinck, J. Dieleman: Appl. Phys. Lett. **55**, 1312 (1989)

VI.15 D.M. Eigler, E.K. Schweizer: Nature **344**, 524 (1990)

VI.16 G. Meyer, B. Neu, K.-H. Rieder: Appl. Phys. A **60**, 343 (1995)

VI.17 M.F. Crommie, C.P. Lutz, D.M. Eigler: Science **262**, 218 (1993)

Panel VII

Surface Extended X-Ray Absorption Fine Structure (SEXAFS)

Besides ion scattering, scanning tunneling microscopy (Panel VI: Chap. 3) and LEED intensity analysis (Sect. 4.4, Panel VIII: Chap. 4), Surface Extended X-ray Absorption Fine Structure (SEXAFS) measurements have become a major source of information about surface atomic structure [VII.1–VII.3]. In principle, the technique is an indirect surface-sensitive measurement of the X-ray absorption in the energy range up to about 10 keV. Before discussing SEXAFS it is thus useful to examine the more direct technique EXAFS, which, from the experimental point of view, is a straightforward X-ray absorption measurement [VII.4]. Since such an absorption measurement is not particularly sensitive to the topmost atomic layers, EXAFS is generally used to study the bulk atomic structure, i.e. bond length and coordination numbers of materials. Figure VII.1 presents a typical K-shell absorption spectrum of Cu [VII.5]. The insert is a schematic absorption spectrum over a wide range of photon energies. The absorption coefficient $\mu(\hbar\omega)$ for X-rays, defined by the exponential decay law of the intensity

$$I = I_0 \mathrm{e}^{-\mu x}, \tag{VII.1}$$

decreases monotonically with photon energy except at absorption edges (L_{I}, L_{II}, ..., K ...) where the photon energy reaches the ionization energy of a particular atomic shell; photoelectrons are produced and a steep edge, i.e. a strong enhancement of the absorption occurs. In condensed matter the absorption coefficient on the high-energy side of this excition edge exhibits a characteristic oscillatory fine structure which is clearly seen in Fig. VII.1 for the K-absorption edge of Cu. The origin of this fine structure is an interference effect of the photoelectron wave function (Fig. VII.2). The photoelectron produced by the ionization of a particular atom is scattered from neighboring atoms. The direct outgoing wave ψ_0 and the waves ψ_{s} backscattered from the various neighboring atoms superimpose to yield the final state of the excitation. The overlap, i.e. the interference condition of this total final-state wave function with that of the core level initial-state wave function changes with photon energy depending on the phase difference between ψ_0 and ψ_{s}, thus causing the observed variations in $\mu(\hbar\omega)$. The absorption coefficient μ is conveniently expressed as

$$\mu = \mu_{0\mathrm{K}}(1 + \chi) + \mu_0. \tag{VII.2}$$

Fig. VII.1 K-shell X-ray absorption coefficient μ of Cu versus X-ray photon energy. Insert: qualitative overview of the absorption coefficient $\mu(\hbar\omega)$ for a wide range of photon energies covering two L edges and one K edge [VII.5]

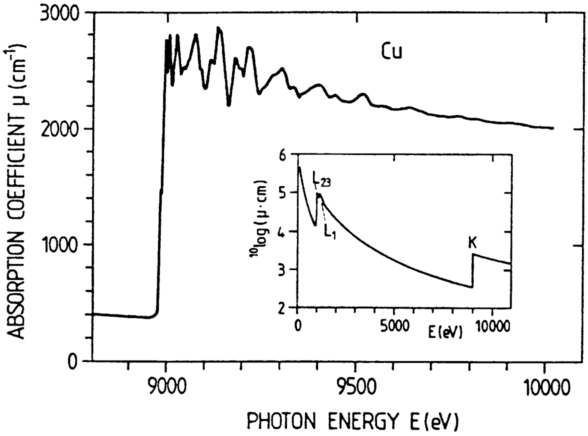

Fig. VII.2 The EXAFS mechanism (schematic). The final-state wave function is a superposition of the unscattered outgoing wave ψ_0 and waves ψ_s that are backscattered from the neighbors of the atom that has been photoexcited

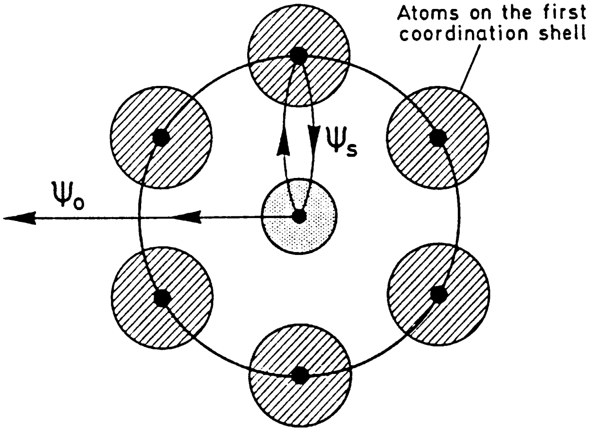

where μ_{0K} and μ_0 are monotonic functions due to K shell excitation (μ_{0K}) and excitation of weaker bound L and M electrons (μ_0). The structural information, i.e. bond length and coordination numbers are then contained in χ. According to the experimental data (Fig. VII.1) χ is a function of photon energy $\hbar\omega$, but because of energy conservation in the photoexcitation process, i.e.

$$\frac{\hbar^2 k^2}{2m} = \hbar\omega - E_B + V_0, \tag{VII.3}$$

one can also express χ as a function of the wave vector k. In (VII.3) E_B is the binding energy of the electron in its initial state, and V_0 the inner potential of the solid (the photoelectron is excited in this potential rather than into vacuum). V_0 is usually not well known and for the data analysis a reasonable estimate is taken. A theoretical expression for $\chi(k)$ is calculated using dipole matrix elements between the initial K-shell wave function and the superposition of ψ_0 (outgoing wave) and ψ_s (waves backscattered from neighboring atoms):

$$\chi(k) = \sum_i A_i(k) \sin[2kR_i + \rho_i(k)]. \tag{VII.4}$$

This expression contains the structure of the photoelectron final state due to interference between ψ_0 and several other waves reflected from neighboring atoms at a distance $2R_i$ (Fig. VII.2). The distance of travel in the interference term is therefore $2R_i$. A number N_i of identical scatterers are grouped together at a distance R_i in a scattering shell. The scattering phase $\rho_i(k)$ at the ith neighbor takes into account the influence of the absorbing and scattering potentials on the photoelectron wave. The EXAFS amplitudes $A_i(k)$ are proportional to the backscattering amplitudes of the surrounding atoms. They allow one to distinguish between different neighbors. Furthermore thermal vibrational amplitudes and damping due to inelastic scattering of the photoelectrons are contained in $A_i(k)$.

Figure VII.3 illustrates qualitatively how the fine structure reacts to variations in the nearest neighbor distance R_i and in the coordination number. For smaller R_i the first maximum occurs at shorter wavelengths, i.e. higher photon energies. Higher coordination increases the number of scatterers and thus the oscillation amplitude.

The analysis of EXAFS data includes several steps: the smooth decreasing background $\mu_{0\mathrm{K}}$ in the absorption coefficient (VII.2) is substracted and the oscillating term χ amplified and recorded taking its average value as the zero line. In the simplest case R_i can be obtained according to (VII.4) simply from the energetic

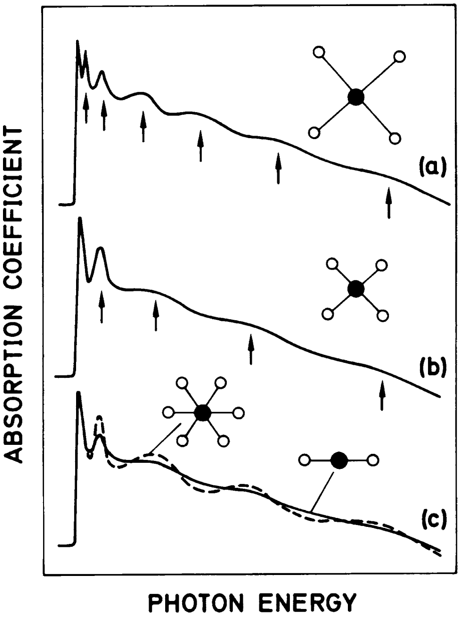

Fig. VII.3 a–c Influence of different bonding geometries on the EXAFS oscillations (qualitative). A larger bonding length decreases the oscillation period (**a, b**); a greater number of scatterers increases the oscillation amplitude (**c**)

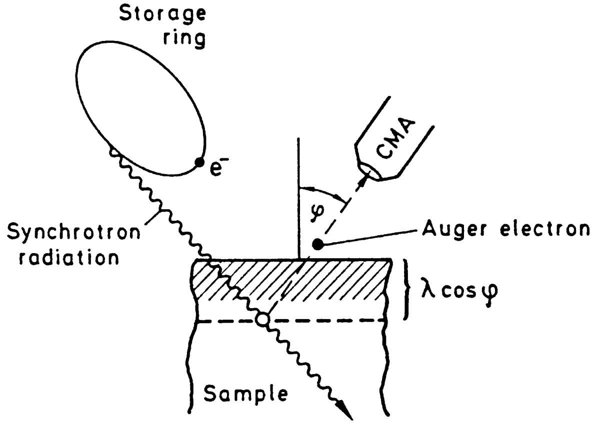

Fig. VII.4 Experimental set-up for SEXAFS. Polarized synchrotron radiation is used as the light source and the Auger yield or secondary partial yield is measured by a CMA. The information depth is essentially given by the projection of the mean-free path λ of the electrons

separation ΔE between the first maximum and the first minimum $[R_i/\text{Å} \approx (151/\Delta E)^{1/2}$; ΔE in eV]. To achieve better accuracy the measured $\chi(k)$ is Fourier-transformed according to

$$F(r) = \frac{1}{\sqrt{2\pi}} \int_{k_{\min}}^{k_{\max}} \chi(k) W(k) k^3 e^{2ikr} \, d(2k). \tag{VII.5}$$

Maxima in $F(r)$ then correspond to the major oscillation periods in $\chi(k)$ and indicate the sequence of distance R_i of shells of neighbors.

In (VII.5) the factor k^3 compensates for the rapid decrease of $\chi(k)$ at large k values. The window function $W(k)$ is used to smooth $\chi(k)$ at the boundaries $k_{\min}$ and $k_{\max}$ in order to avoid artificial side bands in $F(r)$.

Up to this point EXAFS is not a surface-sensitive technique; adsorbate overlayers or the topmost atomic layers of a solid give only a small, frequently negligible, contribution to the total X-ray absorption. Instead of measuring the absorption coefficient μ directly, one can also record any deexcitation product of the photoionization process. This is an indirect way to measure μ; the absorption coefficient is proportional to the probability of ionization, i.e. of producing a hole in the K (or L) shell. Every process for which the probability is proportional to the deexcitation of that hole can be used to measure the absorption coefficient. Possible deexciation channels are the emission of an X-ray photon or the emission of an Auger electron (Panel III: Chap. 2). EXAFS becomes a surface-sensitive method – then called SEXAFS – when the photoemitted Auger electrons are recorded by means of an electron analyser and a detector, or without any analyser simply by means of a channeltron. The surface sensitivity arises from the limited escape depth of the Auger electrons (Fig. 4.1). Because of inelastic interactions (excitation of plasmons, etc.) the average free path of electrons varies between a few Ångstroms and about 100 Å for electron energies between 20 eV and a few keV. The surface sensitivity is particularly high if only electrons from a depth of a few Ångstroms below the surface contribute to the measured yield. As light source, a tunable high intensity X-ray source is necessary. Synchrotron radiation from storage rings is ideal. Figure VII.4

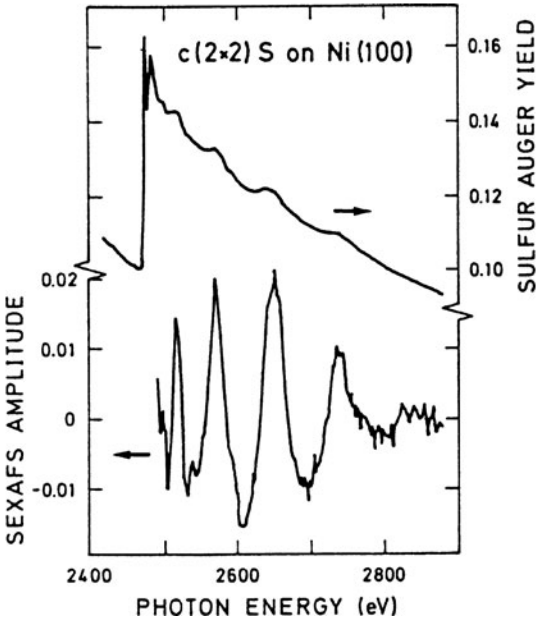

Fig. VII.5 Sulfur K-edge SEXAFS spectrum for half a monolayer of sulfur on Ni(100) [c(2 × 2) LEED pattern] recorded at 45° X-ray incidence. The SEXAFS oscillations after background subtraction are shown in the lower half [VII.6]

shows schematically such an experimental set-up for SEXAFS studies at a storage ring. As in AES, a CMA (Panel II: Chap. 2) is used as electron analyser: its energy window is typically set at energies between 20 and 100 eV to ensure maximum surface sensitivity.

As an experimental example we consider a SEXAFS study of sulfur (S) adsorption on Ni(100) [VII.6]. Figure VII.5 shows the corresponding Auger electron yield measured by means of a CMA. The sample was held at room temperature during adsorption and during the measurement. The energy window of the CMA was fixed at 2100 eV near the KLL-transition of S and measurements were performed with angles of incidence of the synchrotron X-ray beam of 10°, 45° and 90°. The complex Fourier transform $F(r)$, in particular $|F(r)|$ and $\mathrm{Im}\{F(r)\}$, of the measured SEXAFS oscillations (Fig. VII.6) clearly exhibits two main features. Peak A at 2.23 ± 0.02 Å corresponds to the S–Ni neighbor distance whereas peak B indicates that the second neighbor distance is 4.15 ± 0.10 Å. From other measurements it is known that the bulk S–Ni distance in NiS is 2.3944 ± 0.0003 Å. The S–Ni separation for the adsorbed S layer on Ni(100) is thus smaller by 0.16 ± 0.02 Å.

Additional information is needed to yield an unequivocal structure model for the site geometry of the adsorbed S atoms. Taking into account the c(2 × 2) superstructure observed in LEED there are three different possibilities for S adsorption sites. Considering also the intensities of the Fourier bands and using information about the scattering phases, etc., the only remaining possibility is a fourfold coordinated site, where an S atom forms the top of a pyramid whose rectangular basis is formed by four surface-layer Ni atoms.

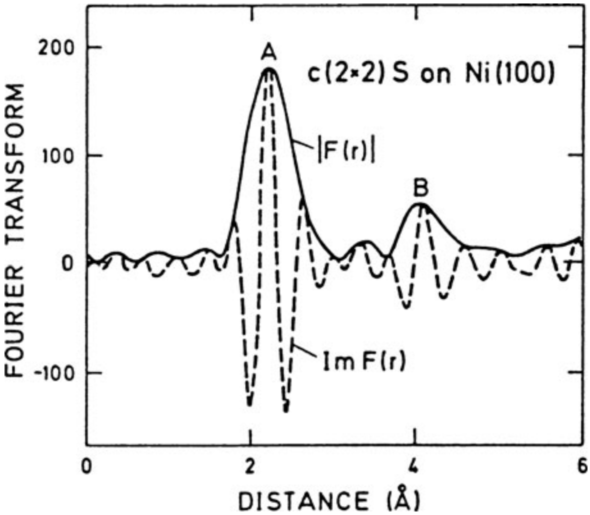

Fig. VII.6 Absolute magnitude (solid line) and imaginary part (dashed) of the Fourier transform of the SEXAFS signal for c(2 × 2) S on Ni(100) recorded at 90° X-ray incidence. Peaks *A* and *B* correspond to S–Ni nearest neighbor and second nearest neighbor distances, respectively [VII.6]

References

VII.1 P.A. Lee, P.H. Citrin, P. Eisenberger, B.M. Kincaid: Extended X-ray absorption fine structure – its strengths and limitations as a structure tool. Rev. Mod. Phys. **53**, 769 (1981)
VII.2 B. Lengeler: Adv. Solid State Phys. **29**, 53 (1989)
VII.3 D. Koningsberger, R. Pries (eds.): *Principles, Techniques and Applications of EXAFS, SEXAFS and XANES* (Wiley, New York 1988)
J. Stöhr: *NEXAFS Spectroscopy*, Springer Ser. Surf. Sci., Vol. 25 (Springer, Berlin, Heidelberg 1992)
VII.4 B.K. Agarwal: *X-Ray Spectroscopy*, 2nd edn., Springer Ser. Opt. Sci., Vol. 15 (Springer, Berlin, Heidelberg 1991)
VII.5 B. Lengeler (ISI, Research Center Jülich): Priv. commun. (1991)
VII.6 S. Brennan, J. Stöhr, R. Jäger: Phys. Rev. B **24**, 4871(1981)

Problems

Problem 3.1 Prove that in two-dimensional Bravais lattices an n-fold rotation axis with $n = 5$ or $n \geq 7$ does not exist. Show first that the axis can be chosen to pass through a lattice point. Then argue by "reductio ad absurdum" using the set of points into which the nearest neighbor of the fixed point is taken by the n rotations to construct a point closer to the fixed point than its nearest neighbor.

Problem 3.2 Chemisorption of group-III atoms such as B, Al, Ga and In on Si(111) surface [1/3 of a monolayer coverage on Si(111)-7 × 7] leads to the formation of a $(\sqrt{3} \times \sqrt{3})$R30° superstructure. Construct the corresponding reciprocal lattice vectors and plot the LEED pattern.

Problem 3.3 On a crystal surface with $\langle 100 \rangle$ orientation, the deposition of a thin film in the initial growth mode leads to island formation. The crystalline islands of the deposited film material exhibit surfaces with $\langle 100 \rangle$ and $\langle 110 \rangle$ orientations. Plot different stages of the island growth under the assumption that $\langle 100 \rangle$ is a fast growing surface, whereas the $\langle 110 \rangle$ surfaces are slowly growing ones.

Problem 3.4 Upon co-deposition of arsenic and gallium on Si(111) surfaces an initial exponential decrease of the Auger intensity of the Si(LVV) line at 92 eV is observed as a function of coverage. The intensity decays from the normalized value 1 on the clean surface to 0.6 at a nominal monolayer coverage of GaAs; at higher coverages between 1 and 3 monolayers, saturation occurs and a constant intensity value of 0.55 is reached.

(a) Calculate the mean free path of Si(LVV) Auger electrons in GaAs (lattice constant 5.65 Å).
(b) From experiment, arsenic is known to form a saturation coverage of 0.85 monolayers on Si(111) at typical growth temperatures. Can the described experimental finding be explained in terms of layer-by-layer growth of GaAs on top of this partial arsenic layer?